Surface & Coatings Technology 520 (2026) 133005

Contents lists available at ScienceDirect

Surface & Coatings Technology

journal homepage: www.elsevier.com/locate/surfcoat

Tungsten-induced atypical multilayer growth in a new amorphous Al-Ti-(W) thin films: A key to improve corrosion resistance in saline environment

Issam Lakdhar [a,*], Akram Alhussein [a], Jean-Luc Grosseau-Poussard [c], Corinne Nouveau [b], Aurélien Besnard [d], Juan Creus [c]

[a] LASMIS, Université de Technologie de Troyes, Pôle Technologique Sud Champagne, 26 rue Lavoisier, 52800, Nogent, France
[b] Arts et Métiers Paris Institute of Technology, LaBoMaP, 13 Rue Porte de Paris, 71250 Cluny, France
[c] LaSIE, UMR 7356 CNRS, La Rochelle Université, Av. Michel Crépeau, F-17042, La Rochelle, France
[d] Université Marie et Louis Pasteur, SUPMICROTECH, CNRS, Institut FEMTO-ST, F-25000, Besançon, France

ARTICLE INFO

Keywords:
Co-sputtering PVD
Al-Ti-(W) thin film
Amorphous structure
Nanometric multilayered growth
Corrosion resistance

ABSTRACT

New Al-Ti-(W) thin films were deposited on 100C6 steel substrates using co-sputtering system, achieving an amorphous structure up to 17 at.% tungsten content. The introduction of tungsten in the film led to a unique and atypical nanometric multilayered film growth with a uniform periodicity of about 2.9 nm, for a tungsten incorporation of 17 at.%. An experimental method was used to confirm the multilayer growth and to determine the growth mode of the other compositions (0, 4, and 11 at.%). This experimental approach was confirmed through simulation method. The open circuit potential (OCP) values of Al-Ti-(W) thin films in NaCl solution were more noble than the bare steel, acting as a cathodic protector in case of galvanic coupling. Cycling polarization, long-term immersion tests, and electrochemical impedance spectroscopy, combined with electrochemical modeling, were employed to evaluate the corrosion behavior of amorphous Al–Ti–(W) coatings on 100C6 steel. The incorporation of tungsten significantly reduces open porosity, a trend confirmed by EIS modeling, which reveals increased pore resistance consistent with a multilayer growth mode that densifies the coatings. The 11 at.% W coating exhibits the lowest corrosion current density, the highest polarization resistance, and the most stable passive regime. Long-term immersion and impedance analyses confirm improved resistance to localized corrosion through passive film formation and partial pore sealing. Raman spectroscopy corroborates these findings by showing corrosion product evolution toward more protective oxides for tungsten rich coatings.

1. Introduction

Corrosion is a spontaneous phenomenon that negatively impacts metals and alloys properties when they are exposed to agressive environments [1,2]. This phenomenon generates substantial economic costs worldwide, leading to find solutions to protect against it [3] and reduces the risks of safety and economic losses [4,5].

Numerous studies have been published in the literature with the objective of understanding corrosion mechanisms of metals and alloys. In their studies, A. K. Ralston et al. were interested to understand the influence of grain size and precipitate size on the corrosion resistance of aluminum based alloys [6–9]. They found a link between grain size and corrosion rate, suggesting that finer grains improve the material durability. Using experimental techniques such as Transmission Electron Microscopy (TEM) and electrochemical tests, they showed that precipitates within a critical size of 3 to 8 nm can affect mechanical strength and complicate the formation of the passive layers. They concluded that the treatment method used to reduce the material grain size influences the corrosion response, as it causes a displacement of elements and modify the grain boundaries nature. This phenomenon promotes the pitting corrosion instead of intergranular corrosion [10].

Environment modifications (conditions such as pH and temperature can be altered, corrosion inhibitors can be introduced) [11], potential changes (anodic and cathodic protections can be employed) [12], and the use of protective non-organic coatings can be applied using a variety of technologies (electrochemical [13,14], Chemical Vapor Deposition

* Corresponding author.
E-mail address: lakderissam@gmail.com (I. Lakdhar).

https://doi.org/10.1016/j.surfcoat.2025.133005
Received 25 September 2025; Received in revised form 17 November 2025; Accepted 27 November 2025
Available online 28 November 2025

(CVD) [15,16], Atomic Layer Deposition (ALD) [17,18], Physical Vapor Deposition (PVD) [19–21]). These methods have been widely tested to reduce the impact of corrosion and protect the metallic substrate from degradation in aggressive environments.

PVD sputtering technique is known with its ability to produce a wide range of materials such as alloys, oxides, nitrides, as monolayers and multilayers [22]. It has been widely validated through testing, particularly for the development of corrosion-resistant coatings [23,24]. Furthermore, Creus et al. studied the corrosion behavior, in saline solution, of various aluminum based alloys and nitride thin films, obtained by electron beam physical vapor deposition (EBPVD) and co-sputtering techniques. The results showed that the incorporation of transition metals modifies the electrochemical characteristics. A reactivity classification of the various thin films was obtained, helping to choose the appropriate coating to use in such applications [25].

PVD is known for its precision in alloy development, enabling the achievement of highly accurate compositions using the co-sputtering technique with different material targets. In addition, a major advantage is its capacity to produce amorphous structures due to the non-equilibrium thermodynamic conditions and the extremely high cooling rate during the transition of adatoms from the vapor phase to the solid state on the substrate [26]. This rapid cooling, in conjunction with other criteria [27], can produce disordered thin film when the desired coatings are metallic.

Amorphous materials, either in bulk form or as thin films, are known for their high corrosion resistance. In recent decades, amorphous structures with various chemical elements have been tested as corrosion barrier coatings [28,29]. The results show that, due to the absence of crystallinity defects and the homogeneity of the material, these coatings exhibit superior resistance to both general corrosion and localized pitting corrosion compared to crystalline structures with the same composition [30].

The aluminum-titanium alloy produced by PVD technique exhibits a composition range where the alloy structure is amorphous. Yan et al. [31] were the first who developed this binary alloy structuration with varying titanium contents. They determined that the amorphous structure was achieved for titanium incorporation ranging between 30 and 60 at.%. Subsequently, other researchers such as Abe et al. [32], Senkov et al. [33], and Kim et al. [34] continued the investigation of this compound. The amorphous structure was confirmed through the application of diverse characterization techniques such as X-ray diffraction, transmission electron microscopy, and differential scanning calorimetry. Investigations were also conducted into the alloy's properties, including its thermal stability, the phases formed during crystallization and its electrical resistivity. Sanchette et al. [35] studied the mechanical and electrochemical properties of the Al—Ti binary alloy with varying compositions. The highest mechanical value was obtained for the amorphous structure. In NaCl solution, the corrosion behavior of the Al—Ti alloy evolved from sacrificial protection (for a titanium content below 30 at.%) to cathodic protection in the amorphous zone when the titanium content increases, in the case of galvanic coupling. In addition to the dense morphology, these properties indicated that it would be an appropriate base matrix for the development of a new ternary alloy doped with tungsten, i.e. Al-Ti-(W), in thin film form, as discussed in a previous article [36]. Indeed, tungsten has been used in numerous studies for various reasons. Known for its hardness, it has been applied to enhance the mechanical strength of coatings and improve other properties, such as hydrogen embrittelement and corrosion resistance [37–40].

In our previous study [36], the Al-Ti-(W) amorphous alloy was tested as a hydrogen barrier. The purpose of the present paper is to investigate the localized corrosion behavior of this alloy and its ability to protect steel. In particular, it is focused on the contribution of tungsten incorporation as an inhibitor and its potential impact on the coating performance through atomic-scale characterization and corrosion tests.

2. Experimental details

2.1. Elaboration conditions

Al-Ti-(W) coatings deposition on the 100C6 steel samples was performed using a DEPHIS4 machine. The 100C6 steel used in this study is characterized by a high carbon content and is known for its good mechanical properties and high wear resistance [41]. Fig. 1.a and b show the chamber enclosure, which contains four 8″ circular cathodes and one shutter generally used for target cleaning. Three pure targets (titanium, aluminum, and tungsten, (99.9 %)) used to elaborate the ternary thin film alloy were positioned as mentioned in Fig. 1.b. The elaboration parameters were the same as those previously optimised and used in our previous article [36], and are presented in the following Table 1. It is noteworthy that the maximum substrate-holder rotation rate was used to ensure a good atomic homogeneity of the alloy. The low vacuum pressure was selected to reduce the presence of impurities in the sputtering atmosphere, preventing any potential impact of these elements on the research outcomes. The other parameters, including the applied current density, deposition rate and time, and the alloy composition with varying tungsten content (0, 4, 11, and 17 at.% W, while Ti/Al ratio remains constant at around 0.84), are mentioned in the Table 2.

2.2. Characterization techniques

2.2.1. Characterization of morphology and microstructure of thin films

The coated samples and the bare 100C6 steel were analyzed by X-ray diffraction using a Brucker D8 Advance machine. The diffractometer is equipped with a copper tube radiation source with a wavelength $\lambda_{cu} =$ 0.154 nm. It is operated at a power of 1600 W ($I = 40$ mA, $V = 40$ kV). All measurements were carried out with a scan step of 0.02° and a step time of 1 s using Θ-2Θ mode and a 2Θ diffraction angle ranging from 20 to 150°.

The growth morphology of the coatings was examined using a FEG Hitachi SU 8030 scanning electron microscope (SEM), while the thickness of the coatings was measured using a profilometer Altisurf 500. The compositional analysis of thin films was performed using Energy Dispersive X-ray Spectroscopy (EDX).

To study the microstructure of the coatings at the nanometric and atomic scale, a JEM-ARM 200F cold FEG TEM was used. The microscope is operated at 200 kV using a spherical aberration (Cs) probe and image correctors, with a point resolution of 0.12 nm in TEM mode and 0.078 nm in STEM mode. Before TEM analysis, a Focused Ion Beam (FIB) lamella was prepared using an MEB-FIB Helios NanoLab 600i. A protective platinum layer was deposited on the surface prior to cutting and thinning the lamella to a thickness of less than 100 nm.

2.2.2. Characterization of corrosion performance of thin films

Corrosion tests were carried out in a flat cell containing 250 ml of a 3 wt% NaCl solution (pH = 7) at ambient temperature and in an aerated environment. A conventional three-electrode electrochemical setup was used, with a saturated calomel reference electrode (SCE), a platinum grid as counter electrode, and a working electrode represented by the bare and coated substrate. Two configurations used for studying the intrinsic open circuit potential (OCP) behavior of Al-Ti-(W) thin films deposited on glass slides and for examining the electrochemical performance of bare and coated 100C6 steel. The exposed surface area is 1 cm^2. The electrochemical cell is connected to an Origalys potentiostat-galvanostat. To ensure the consistency and uniformity of the experimental conditions, the same experimental setup was employed for all experiments, regardless of the composition of the exposed surface.

The objective of the potentiodynamic tests was to identify the corrosion behavior of Al-Ti-(W) thin films. OCP test was conducted for one hour, followed by a cyclic polarization test under the following conditions: potential start from −0.1 V/OCP to 1 V/ECS at a scan rate of 0.5 mV/s. This methodology enables the determination of diverse

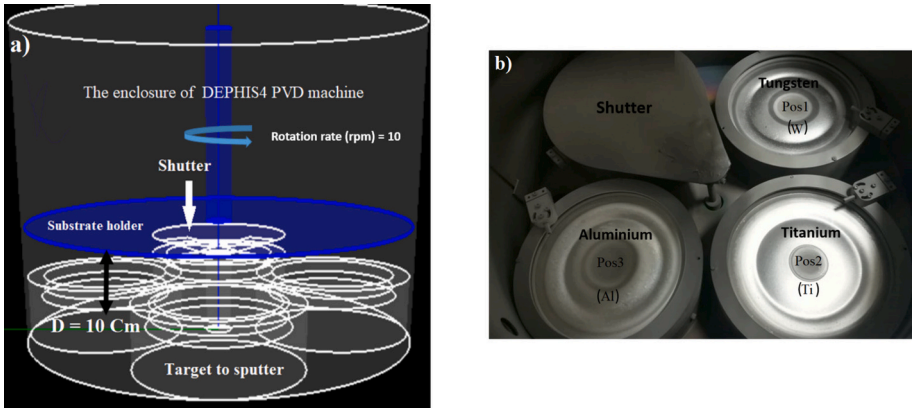

Fig. 1. (a) PVD machine DEPHIS4 design using SIMTRA [42] software. (b) Targets position used for the deposition of Al-Ti-(W) ternary coatings.

Table 1
Experimental parameters of the Al-Ti-(W) deposition.

Parameters	Value
Vacuum pressure (Pa)	6.10^{-4}
Working pressure (Pa)	0.3
Argon gas flow (sccm)	100
Substrate holder-target distance (cm)	10
Substrate holder rotation rate (rpm)	10
Temperature (°C)	Floating temperature

Table 2
Essential parameters for achieving 4 µm thick thin films with tungsten incorporation.

Samples	S0	S1	S2	S3
W content (at.%)	0	4	11	17
I_W (A)	0	0.2	0.4	0.8
I_{Al} (A)		1.66		
I_{Ti} (A)		2.7		
Deposition rate (µm.h^{-1})	1.35	1.41	1.61	1.75
Deposition time (min)	176	170	148	138

corrosion modes occurring on the surface of samples exposed to a corrosive chloride environment. A reverse scan was performed to evaluate the post-corrosion behavior of the samples by reversing the potential path once a current threshold of 1 mA/cm^2 was reached, continuing to a starting potential of −0.1 V/OCP. A linear polarization measurements over a narrow potential range of ±20 mV/OCP at a scan rate of 0.2 mV/s was caried out in order to allow the determination of the polarization resistance. To better understand the corrosion behavior of the coatings and evaluate their performance, long-term immersion tests were carried out. The open-circuit potential (OCP) was monitored over a period of 72 h (3 days). A punctual polarization resistance measurements (Rp) were carried out by applying a potential sweep of ±20 mV/OCP at a scan rate of 0.2 mV/s for immersion time of 1 h, 8 h, 13 h, 24 h, 36 h, 48 h, 60 h and 72 h. To further clarify the degradation mechanisms of the coatings, electrochemical impedance spectroscopy (EIS) was performed during complete immersion in a saline solution for 72 h. The EIS measurements were conducted at the open-circuit potential, using a potential amplitude of 10 mV and a frequency range from 60 kHz to 10 mHz. Measurements were taken after 1 h, 8 h, 24 h, and 72 h of immersion. The experimental data were fitted using an equivalent electrical circuit, which helps describe the physical phenomena occurring during corrosion. The circuit parameters were obtained using the ZView software.

Optical observation of the exposed area was performed using an optical microscope Keyence VH Z250R. µ-Raman analysis was carried out with a LabRAM HR High-Resolution Raman spectrometer (Horiba) equipped with an Olympus BX41 microscope and a Peltier-based cooled charge-coupled device (CCD) detector. The analyzed zones were observed at a magnification of ×50 giving rise to a lateral resolution of a few micrometers. Spectra were acquired at room temperature via the LabSpec 6 software with a spectral resolution of 0.1 cm^{-1}. The excitation was provided by a green laser (λ = 532 nm). Its power was reduced to 0.23 mW (2,5 % of the maximal power) in order to prevent excessive heating of the analyzed compounds. The acquisition time was equal to 60 s and as µ-Raman provides a local analysis, various zones were analyzed to get representative results.

3. Results and discussion

3.1. Microstructure analysis

XRD patterns of the bare 100C6 steel and the coated samples with different Al-Ti-(W) thin film compositions are presented in Fig. 2. The uncoated steel shows a martensitic structure, displaying a predominant X-ray diffraction peak at 2Θ value of 44° for the (110) plane and additional secondary peaks at 65° for the (200) plane and at 82° for the (211) plane. The diffraction patterns of the coated steel with Al-Ti-(W) thin films exhibit the same crystalline peaks as the bare steel, with lower peak intensities and a broad peak in the 2θ range from 34 to 45°. This confirms the amorphous state of the coatings [36]. As shown in the same figure, the incorporation of tungsten resulted in a broad peak shift to higher 2θ values, indicative of a densification of the amorphous coating. This observation aligns with the findings presented in the previous article, that employed the Ehrenfest formula [43] to elucidate this phenomenon.

3.2. Observation of the morphology of the thin films and investigation of the chemical composition and the formation of nano-layers

3.2.1. Amorphous thin film morphology

The cross-sectional SEM images are presented in Fig. 3. A crack-free, dense morphology for the various Al-Ti-(W) compositions is observed [36].

3.2.2. TEM caracterisation of the Al-Ti-(W (17 at.%)) thin film

Fig. 4.a, b, and c present TEM images of two different areas. The first area corresponds to the interface between the 100C6 steel substrate and the Al-Ti-W (17 at.%) coating, while the second area corresponds to the upper interface between the coating and the platinum layer. Both observations show continuous and same mode growth of the Al-Ti-W (17 at.%) coating in these two areas. Furthermore, the formation of periodic nano-layers is noticed, exhibiting a period thickness of approximately 2.9 nm, as illustrated in Fig. 4.d.

The period thickness was correlated with the amount of material deposited on the substrate during the sputtering of the three targets

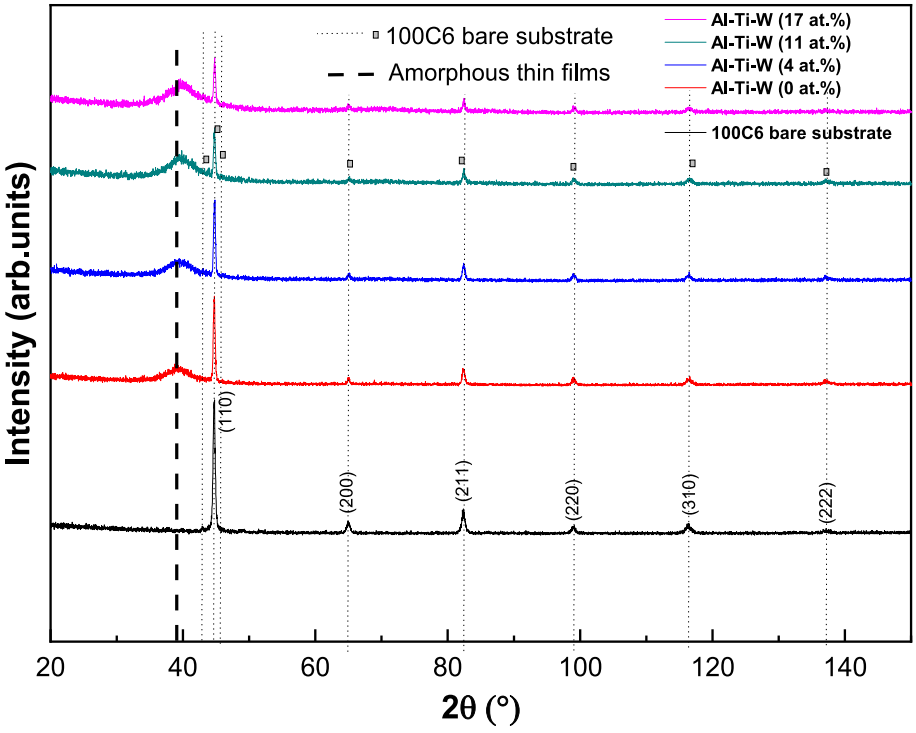

Fig. 2. XRD diffractograms of Al-Ti-(W) alloys deposited on 100C6 steel.

(aluminum, titanium, and tungsten) over the course of one complete rotation of the substrate holder. The deposition time (T) for the Al-Ti-W (17 at.%) ternary composition was 138 min (Table 2) to achieve a film thickness (eF) of approximately 4 μm. The rotation of the substrate holder was set to a maximum value of 10 rotations per minute to ensure optimal homogenization of the coating. Thus, the thickness of the Al-Ti-W (17 at.%) nano-layer deposited on steel per rotation of the substrate holder is calculated using the following formula:

$$e\left(\frac{\text{nm}}{\text{rot}}\right) = \frac{e_F\,(\text{nm})}{T\,(\text{min})*Vr\,(\text{rpm})} \approx \frac{4000}{138*10} = 2,89\ \text{nm}\Big/\text{rot} \quad (1)$$

In the equation, e_F represents the total film thickness in nanometers (nm), T is the deposition time in minutes (min), and Vr refers to the rotation speed of the substrate holder in rotations per minute (rpm).

The calculated nano-layer thickness (2.89 nm), based on the film elaboration parameters, is in close agreement with the measured value obtained from TEM analyses.

A zoom of the diffraction pattern image shows the presence of bright spots aligned in the same direction as the coating growth, as illustrated in Fig. 5.a. These spots are equidistant, with a spacing of approximately 2.88 nm. In order to ascertain the distance between the diffraction planes and the center of the diffraction pattern, which corresponds to the normal direction of the electron beam (zone axis), the distance between the first diffraction plane and the zone axis was calculated and equals to 2.76 nm. As one moves away from the zone axis, the distance between the second diffraction plane and the zone axis was 1.4 nm, while the distance between the third diffraction plane and the zone axis was 0.9 nm.

As shown in Fig. 5.b, these values correlate well with the interplanar distance of diffraction planes belonging to the same family, according to Bragg formula. However, these spots do not correspond to crystalline diffraction planes, but rather to the diffraction of the interfaces between the repetitive nano-layers of the material near the zone axis. In addition, the distance between successive spots matches well with the thickness of a single Al-Ti-W (17 at.%) nano-layer.

Figs. 5, 6, and 7 present high-resolution scanning transmission electron microscopy (STEM) images, primarily in high-angle annular dark field (HAADF) mode. The image shows a gradient of tungsten within the period, manifested as a contrast between bright and dark regions. The bright region indicates an area comprising a greater concentration of heavier constituents than the dark region. Consequently, the region exhibiting a higher concentration of tungsten appears brighter, whereas an absence of tungsten results in a darker appearance.

Fig. 6 shows the chemical composition profile along the thickness of the Al-Ti-W (17 at.%) coating. The Ti/Al ratio remains nearly constant at an average value of 0.87 along the entire line, irrespective of the electron beam position within the period, as it crosses several nanometric periods.

Concerning the tungsten element, the content varies from 24 at.% in the bright regions to 15 at.% in the dark regions as shown in Fig. 6. In a single period, the dark region exhibits a thickness estimated to be approximately 0.9 nm (Fig. 4.d). The beam size utilized for EDX analysis under STEM exceeds one nanometer. Therefore, it is possible that tungsten content in the dark region is significantly lower than 15 at. %, indicating probably a total absence of this element.

X-ray mapping confirmed the heterogeneity in the distribution of tungsten within the Al-Ti-W (17 at.%) coating, as evidenced by the presence of dark fringes corresponding to areas with lower tungsten content (Fig. 7). In contrast, the maps of the other two chemical elements (titanium and aluminum) show a homogeneous distribution within the coating.

3.2.3. *Tungsten induced multilayer growth*

In order to clarify the nanoscale multilayer growth, an experiment was conducted to study the quantity and nature of the elements deposited on a silicon substrate (Fig. 8.b) as the tray was rotated inside the deposition chamber and the three targets aluminum, titanium, and tungsten were sputtered. The rotating substrate-holder enables the position of the substrate to be changed at each instant T until it returns to its initial position. In fact, the substrate occupies an infinite number of positions as it rotates. In our case and to simplify the experiment, 16 substrates were placed on the substrate-holder plate in 16 positions, spaced 12 cm from the center of the plate (the axis of the chamber) and

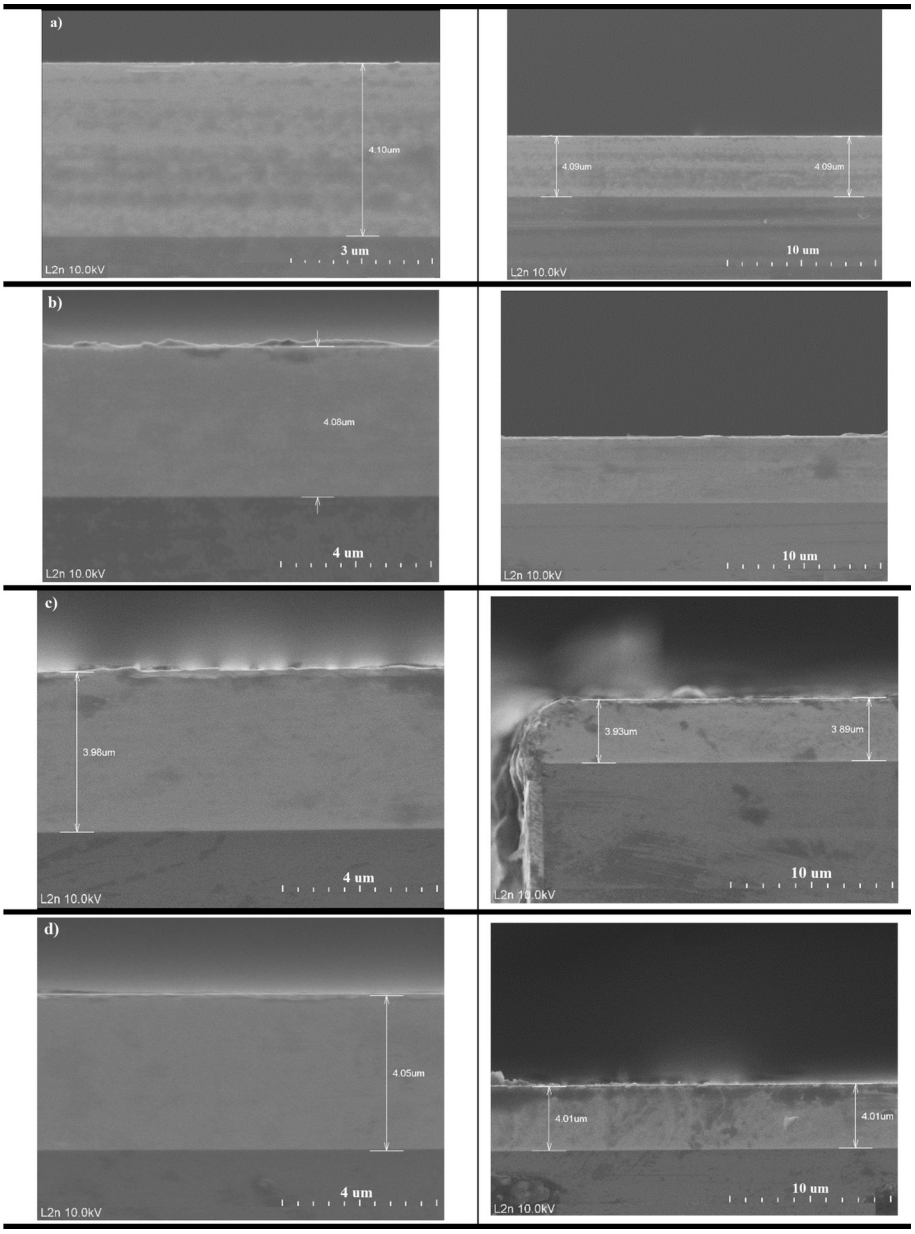

Fig. 3. SEM cross-section images of Al—Ti alloys containing a) 0 at.% W, b) 4 at.% W, c) 11 at.% W, and d) 17 at.% W [36].

22.5° apart from each other, as shown in Fig. 8.a. The same configuration was simulated in SIMTRA on a continuous stripe at the same radius than that of the samples. A ternary Al-Ti-(W) coating (17 at.%) was elaborated under identical operational conditions, with the exception that the substrate-holder was maintained in a fixed position and the substrates were identified by the initial designation P0, which corresponds to the center of the tungsten target, and by an arrow indicating the direction of positioning.

After one hour of sputtering, the coated substrates were analyzed using EDX Spectroscopy to determine the chemical composition of the coating in relation to each position on the substrate-holder. Fig. 9.a (square and triangle symbols) illustrates the experimental variation in atomic percentage of the three elements, aluminum, titanium, and tungsten, based on their respective positions and tuned by a coefficient representative of the thickness of the films. Fig. 9.a (small triangle symbols) illustrates the simulated variation in the fraction of the three elements, aluminum, titanium, and tungsten, based on their respective positions and tuned y a coefficient representative of the composition. As expected, between P10 and P14, the substrates are above the shutter and receive a very limited amount of matter. Consequently, the films are very thin at these positions. The simulation reproduces correctly the variation of the elemental composition along a rotation and confirm the multilayer growth of the film.

The spatial distributions of aluminum and titanium on the platform exhibit a high degree of similarity, as they coexist at the majority of positions with varying quantities. However, tungsten shows a restricted dispersion across the substrates, as it was not detected on substrates positioned between P4 and P11, specifically in the zones above the aluminum target, which is directly at the opposite of the tungsten target and partially above the titanium target. Two factors are responsible for this spatial distribution. The first factor is the elaboration parameters, specifically the current intensities applied to the three targets, which result a broader solid angle for the titanium and aluminum vapor flux compared to tungsten, with current intensities of 2.7 A, 1.66 A, and 0.8 A, respectively. This factor, which was studied by Billard et al., demonstrated that the distribution angle (solid angle) depends on the discharge voltage applied to the target [44]. This hypothesis was confirmed by varying the current intensity applied to the tungsten target

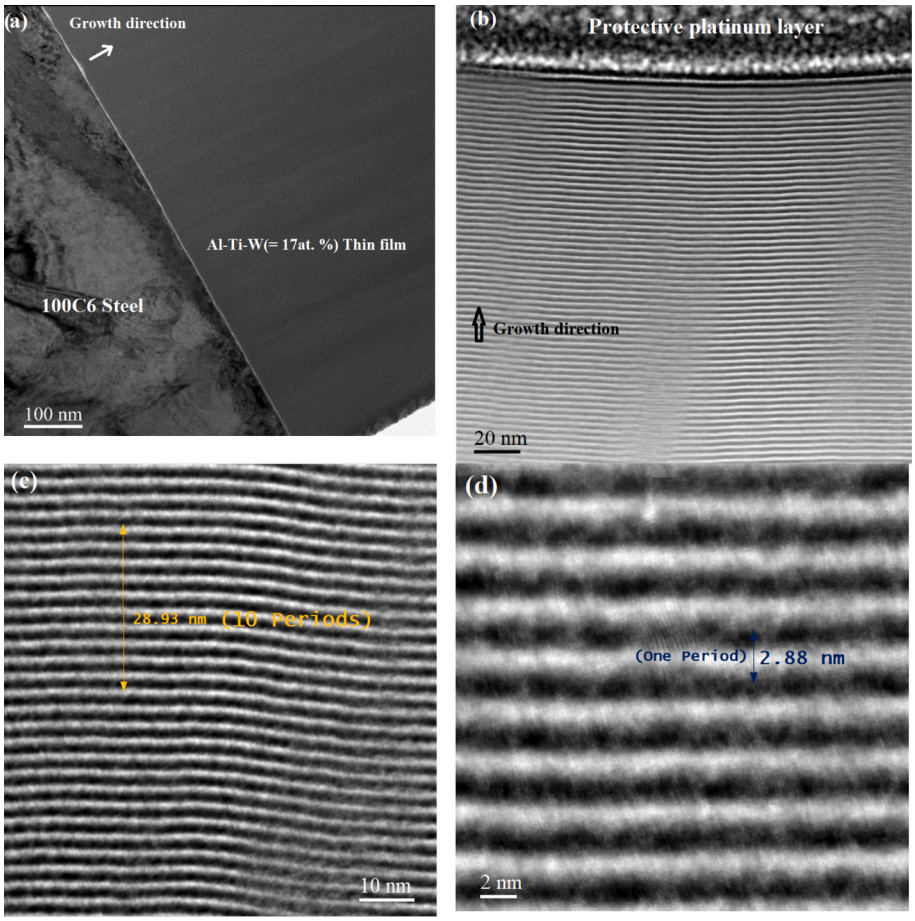

Fig. 4. TEM images of a cross-section of Al-Ti-(W = 17 at.%) coating: (a) layer growth from the 100C6 substrate, (b) at the coating-platinum interface, and (c) and (d) at the center of the layer.

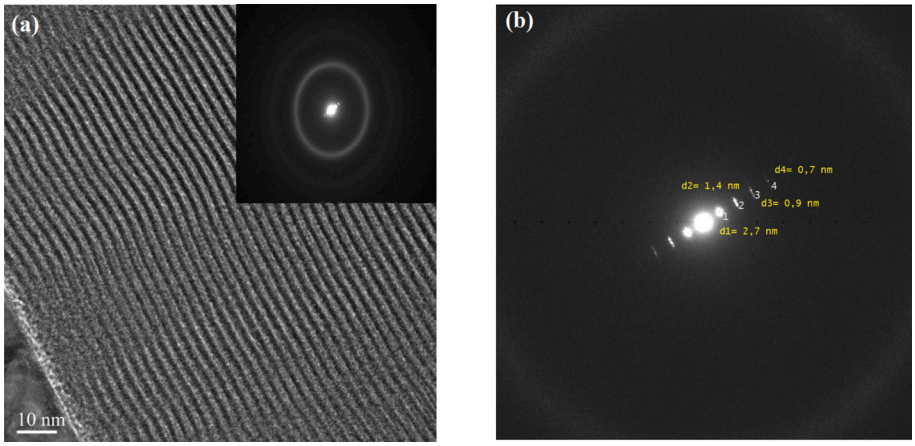

Fig. 5. (a) SAED pattern of the Al-Ti-W (17 at.%) coating associated to cross-section MET image, (b) zoom on the electron diffraction pattern.

from 0.2 to 0.8 A. Fig. 9.b shows the atomic distribution of tungsten at each position relative to the other elements (aluminum and titanium). The results indicate a decrease in the areas where tungsten is absent ($\Delta\varphi$) as the current intensity applied to the targets increases. This factor also explains the narrower distribution for titanium and aluminum in the case of the simulation compared to the experimental. Indeed, only the gas pressure is taken into account in the transport and not the metallic flux, i.e. the current on the targets. If this parameter could be integrated in the simulation titanium and aluminum distribution would be broader, matching perfectly the experimental results.

The second factor is the reduction in the molar mass of the sputtered element, leading to a broader dispersion of the metal vapor flux and it is directly correlated with the deposition rate of the material. Given its highest molar mass among the three elements (183.85 g/mol), tungsten results in a more restricted solid angle of sputtering compared to aluminum and titanium. Therefore, the low incident ion energy (Ar^+) associated with the low current density applied (0.8 A), in conjunction with tungsten high atomic mass, explains the limited dispersion of this element. Consequently, regions of the nanometric period exhibited an absence of tungsten, allowing the presence only aluminum and titanium,

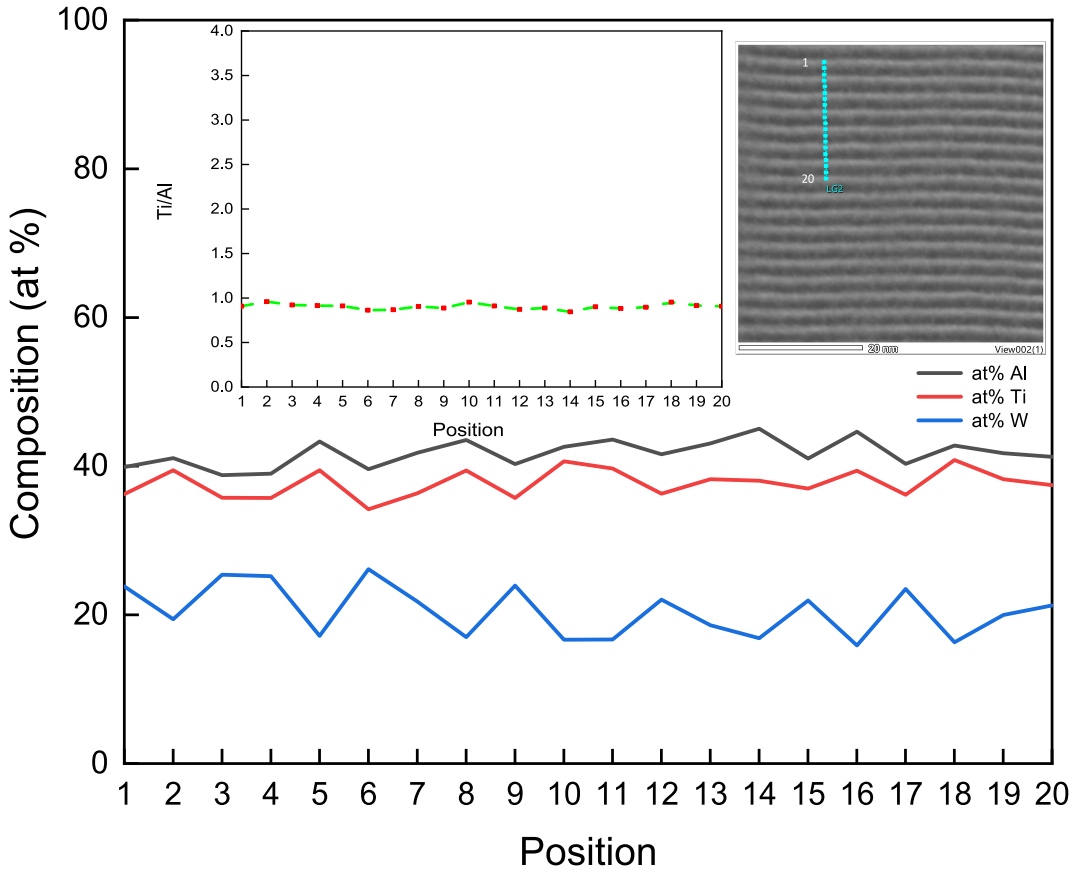

Fig. 6. Chemical composition profile of the Al-Ti-W (17 at.%) coating measured through the film thickness (in cross-section).

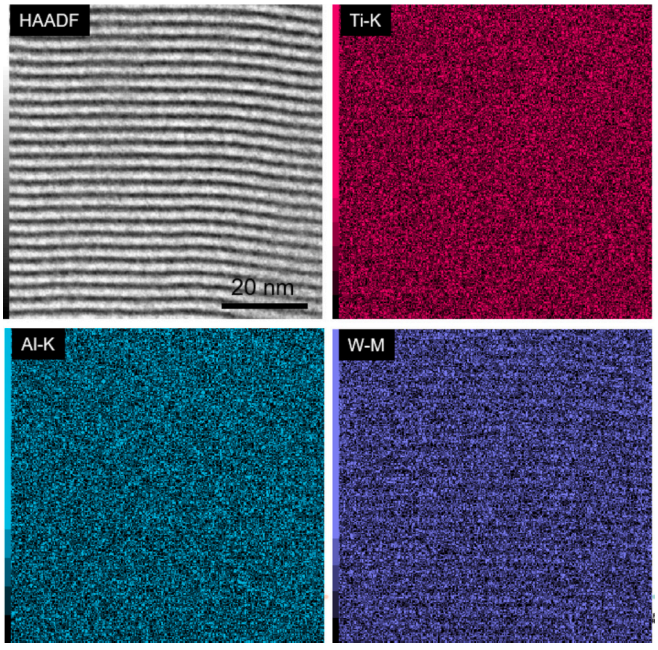

Fig. 7. Aluminum, titanium, and tungsten distribution map in the Al-Ti-W (17 at.%) coating.

which have significantly lower molar masses compared to tungsten. This results in these regions appearing darker in TEM imagery, as previously discussed.

The thickness of the dark zone (*es*) can be calculated from Fig. 9.b by

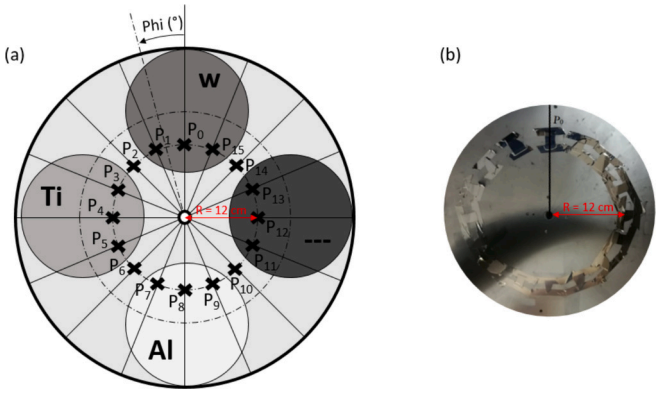

Fig. 8. Schematic view(a) and image(b) of silicon substrates position on the substrate-holder.

using the Eq. (2). The value is very close to those calculated from TEM images using the GATAN software, as mentioned in the Fig. 10.a, confirming our experimental method. Now, knowing the deposition time the (Δφ) to determine the zone where tungsten is absent for the other compositions, we can determine the growth mode of the other compositions (Fig. 10.b). The thickness of the period constituting each composition, the zones where tungsten element is present (*er*) and absent (*es*) and the number of interfaces are presented in the following Table 3.

In Table 3 and Eq. (2), the following notations are used: e_S represents the thickness of the dark zone where tungsten is absent, e_P is the total period thickness, and Δφ is the polar angle associated to the absence of tungsten zone in the thin films.

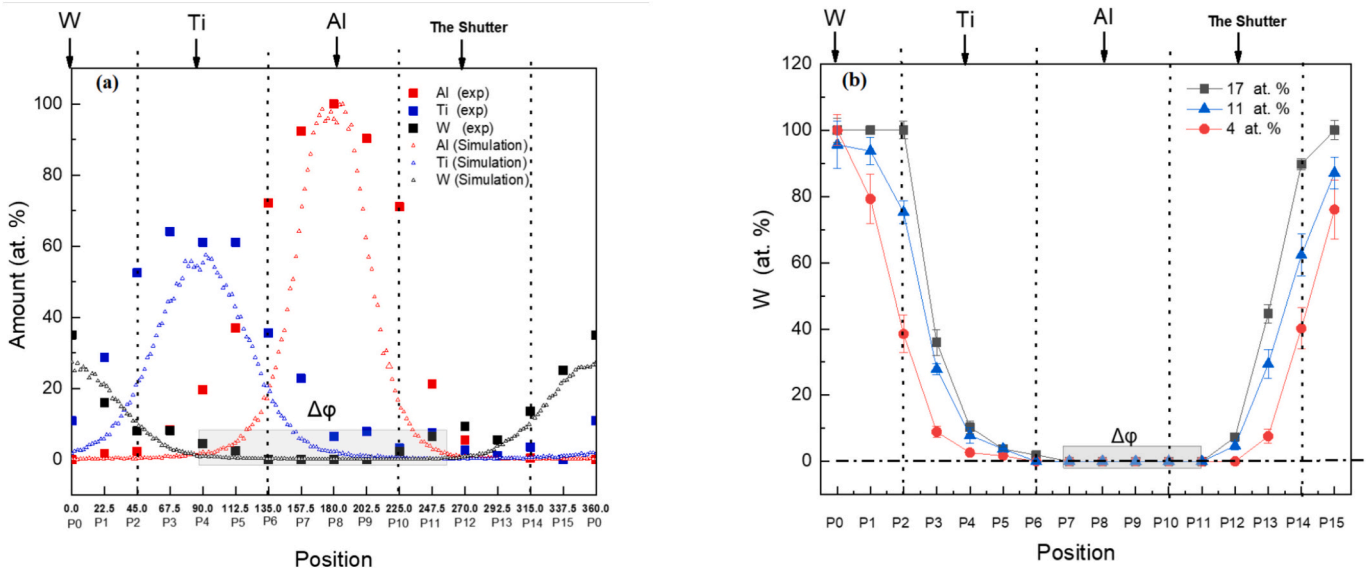

Fig. 9. (a) Spatial dispersion of the metallic vapor of the three elements Al, Ti, and W as a function of Phi (the polar angle of the substrate-holder), and (b) W concentration for different current intensities.

$$e_s = \frac{ep * \Delta\varphi}{360°} = 0.9 \text{ nm} \qquad (2)$$

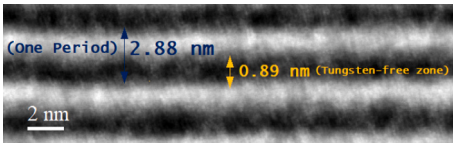

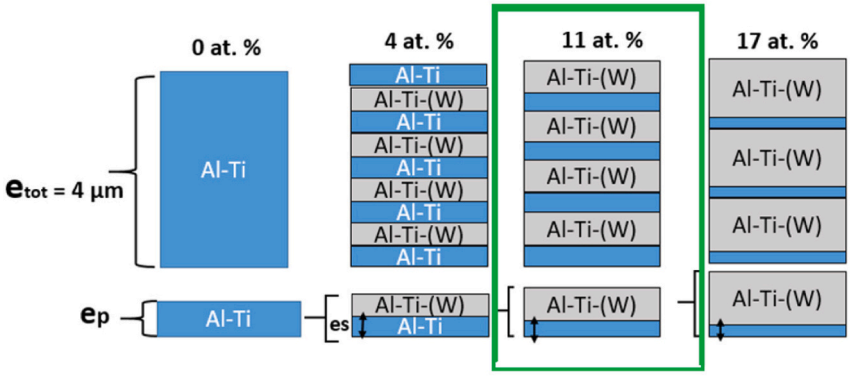

Fig. 10. Growth mode of Al-Ti-(W) thin film amorphous layers with different tungsten contents.

Table 3
Experimental Parameters of the Growth Mode of Amorphous Al-Ti-(W) Thin Films.

W content (at. %)	0	4	11	17
Thickness per period (nm)	2.27	2.35	2.7	2.89
Δφ (°)	–	157.5	135	112.5
e_s (nm)	–	1.02	1.01	0.9
e_a (nm)	–	1.33	1.69	1.99
Number of interfaces	0	3400	2960	2760

Considering the reliability of the experimental approach used to determine the growth mode of amorphous Al-Ti-(W) thin films, we can conclude, as shown in Fig. 10.b, that for the binary base alloy Al—Ti, there is a repeated deposition of material with a thickness of 2.27 nm and a constant Al/Ti ratio. This is further confirmed by nanometric EDX analyses shown in Fig. 6, which indicate a homogeneous distribution of both elements aluminum and titanium throughout all periods. This suggests that the film growth does not generate interfaces. The progressive incorporation of tungsten led to an increase in the amount of material sputtered and deposited on the substrate. This explains the increase in thickness observed during one rotation of the substrate holder (one period) from 2.35 to 2.89 nm for 4 and 17 at.%, respectively. The sputtering of tungsten resulted in the creation of interfaces, as shown in the TEM analyses (Fig. 4.b), due to a compositional variation between tungsten-free zones (es) and tungsten-rich zones (ea). By increasing the amount of tungsten sputtered, the period thickness increases, reducing the number of rotations needed to reach a total thickness of 4 µm and thereby reducing the sputtering time. This results in a decrease in the total number of interfaces in the coating, from 3400 to 2760, as the tungsten content increases from 4 to 17 at.%, respectively. The growth mode of the coating with 11 at.% tungsten, highlighted in green, represents a compromise between a high number of interfaces (compared to 17 at.%) and a higher tungsten content compared to 4 at.%.

4. Electrochemical behavior of Al-Ti-(W) thin film-deposited on steel

4.1. Intrinsic Al-Ti-(W) thin film nature

Fig. 11 shows the evolution of the open circuit potential (OCP) during one hour of immersion for amorphous Al-Ti-(W) on an inert substrate (glass slide). The OCP evolution of 100C6 steel is compared to that of the coated samples to evaluate the behavior of these coatings in the case of galvanic coupling with the 100C6 steel through defects and imperfections existing in the amorphous films.

The steel OCP decreases rapidly from −0.51 to −0.68 V/SCE after 30 min of immersion, subsequently attainting a stable value at the final potential. This behavior is typical for steels in saline solutions and can be attributed to the formation of corrosion products on the surface [45]. The OCPs of Al-Ti-(W) coatings are nobler than that of steel substrate, indicating that these coatings act as a cathode when galvanic corrosion occurs through open defects. The binary Al—Ti coating shows a fast ennoblement of the OCP within the first minutes of immersion, suggesting a rapid passivation of the binary alloy in saline environment. After one hour of immersion, the OCP evolves from −0.36 to −0.2 V/SCE. This behavior is quite similar to that observed for pure titanium coating on an inert substrate [46]. Incorporation of tungsten induces an enoblement of the OCP depending on the microstructure of the ternary alloy. In the case of the coating with 4 at.% of tungsten, the OCP remains stable during immersion. A significant ennoblement is observed for the sample containing 11 at.% W. This ennoblement may be related to the higher surface roughness observed in the previous article, leading to an increase in the number of reactive sites, thereby promoting alloy passivation and to multilyered growth mode, which depends to the coating composition. The OCP exhibits a rapid ennoblement and subsequently stabilizes after 30 min of immersion, reaching values of approximately a few mV/SCE.

The OCP for the sample containing 17 at.% W remains stable during the immersion period, exhibiting a value of approximately −0.15 V/SCE. The discrepancy in the coatings behavior can be explained by the multilayer structured coatings observed by TEM analysis.

After identifying the intrinsic nature of the Al-Ti-(W) coatings through the evolution of their OCPs in NaCl solution, a study of the corrosion performance of coated steels was performed.

4.2. Corrosion resistance of Al-Ti-(W) coated 100C6 steel

The initial and final values of the OCP after 1 h of immersion in a saline environment are presented in Table 4.

Table 4
OCP at $t = 0$ and 1 h after immersion of samples in a 3 wt% NaCl solution.

Sample	E_{0h} (V/SCE)	E_{1h} (V/SCE)
100C6 Steel	−0.511	−0.679
Al-Ti	−0.475	−0.551
Al-Ti-W (4 at.%)	−0.529	−0.598
Al-Ti-W (11 at.%)	−0.525	−0.509
Al-Ti-W (17 at.%)	−0.846	−0.715

For the binary Al—Ti coating, the OCP decreases slowly during the immersion period, reaching a value of approximately −0.55 V/SCE after 1 h of immersion. The same behavior was observed in the studies conducted by Sanchette et al. regarding the corrosion behavior of binary Al—Ti alloys obtained through technology Electron Beam (EBPVD) [36,47].

The Al-Ti-(W) coatings exhibit a combination of characteristics with regard to the evolution of the OCP. For a low tungsten content of 4 at. %, the OCP decreases during the first 5 min of immersion and then stabilizes around −600 mV. The evolution of the OCP is comparable to that of the binary Al—Ti alloy, but shifted to values that are more negative. This phenomenon has been attributed to either tungsten incorporation [48] or a higher open defects density.

The increase of the tungsten concentration in the coating (to 11 or 17 at. %) seems to influence the coating immersion behavior. The Al-Ti-W (11 at. %) coating shows an ennoblement of the OCP during immersion, stabilizing at approximately −0.5 V/SCE. This suggests that the open defects sealed during immersion, thereby limiting the galvanic effect between the coating and the steel substrate. The initial OCP of the ternary alloy with 17 at.% W at −0.85 V/SCE is notably lower than the intrinsic initial potential value of the alloy, which was measured at −0.15 V/SCE. This may be related to the particular microstructure of the ternary alloy on the steel substrate. The OCP is observed to ennoble during immersion, yet it remains at more negative values compared to the OCP of 100C6 steel and other coating compositions.

To summarize, The OCP of the Al-Ti-(W) coating is higher than that of steel, which provides insight into the corrosion mechanism of the coated substrate through the open porosity. The OCP evolution may be influenced by a number of factors, including the galvanic coupling between the coating and the steel substrate, the open porosity rate of the layer, the surface topography (roughness), and the nature of the constituent elements of the material. To better understand the degradation mechanism of Al-Ti-(W) alloys and the effect of tungsten incorporation, potentiodynamic tests are necessary.

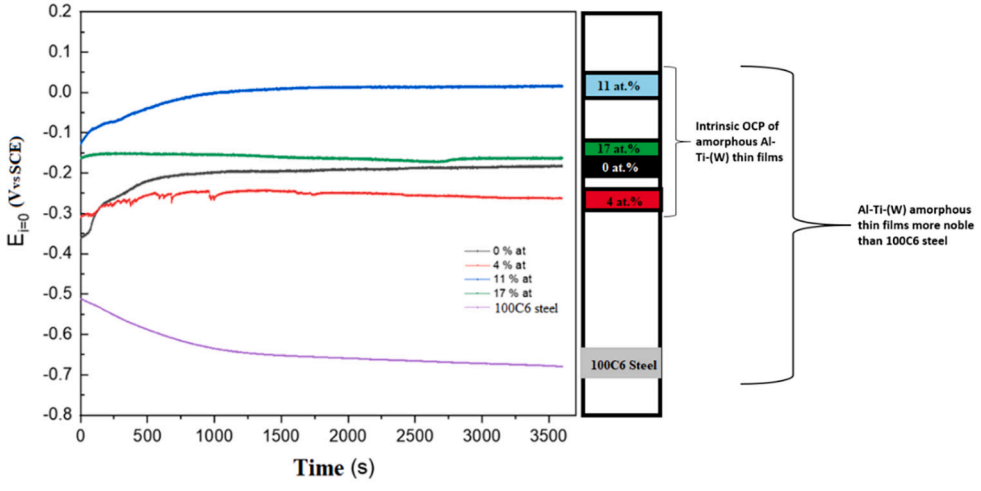

Fig. 11. Evolution of the open circuit potential of amorphous Al-Ti-(W) coatings deposited on glass substrate.

4.2.1. Potentiodynamic behavior of Al-Ti-(W) coated 100C6 steel

Cycling polarization tests were carried out on the steel substrate and Al-Ti-(W) coatings in a NaCl solution at room temperature. These tests permit to determine the corrosion current density using Tafel method as well as other parameters such as corrosion potential, passivation current density, and localized corrosion potential (pitting corrosion). All electrochemical parameters are summarized in Table 5. The linear polarization resistance (Rp), calculated near the corrosion potential, is also illustrated in Table 5.

The polarization curves are presented in Fig. 12. The arrows in the figures indicate the forward and reverse sweep when varying the applied potential.

The polarization curves for the bare 100C6 steel and the coated one with the binary Al—Ti are presented in Fig. 12.a. The bare substrate presents a typical behavior of uniform corrosion, with a corrosion current density of approximately 3 μA/cm^2, a corrosion potential of −0.62 V and a linear polarization resistance of 220 Ω. cm^{-2}. This later value is similar to that reported in the literature [26].

Generally, the degradation of the 100C6 steel is observed to occur with the formation of corrosion products based on iron oxyhydroxide. During the return scan, the same curve shape was observed with a similar return of the corrosion potential. A slight hysteresis was observed during the return scan, which can be attributed to the increase in surface roughness resulting from the oxidation reaction.

The polarization curve of the binary Al—Ti coating shows a distinctive profile when compared to that of the bare 100C6 steel. The corrosion potential was determined to be approximately −538 mV/SCE. This potential is more negative than that of the intrinsic Al—Ti alloy corrosion potential, suggesting an interaction with the steel substrate through the coating open porosities. The current density demonstrates a gradual increase within the anodic range, indicating the localized dissolution of the steel substrate, for a applied potential lower than OCP intrinsic of binary Al—Ti coating (Fig. 12.b), until a passivation "plateau" is reached at approximately −0.1 V/SCE. This behavior is reflective of the Al—Ti alloy, exhibiting a passivation current density of approximately 80 μA/cm^2. Pitting (localized) corrosion is observed at a potential of 0.17 V/SCE. The return scan shows a significant hysteresis and a shift in the return corrosion potential to a more negative value, which can be explained by changes in surface topography. In addition, the return scan reveals the absence of re-passivation for the Al—Ti coating under these polarization conditions. The polarization curves for Al-Ti-(W) coatings on steel substrates are presented in Fig. 12. The incorporation of tungsten into the Al—Ti matrix results in a polarization curve evolution that is similar to that observed in the binary Al—Ti alloy. The electrochemical parameters obtained from these curves are summarized in Table 5. The results demonstrate that tungsten incorporation induces a slight shift in the corrosion potential up to 11 at.% W and a significant reduction in the corrosion current density. Referring to the studies by M. Hou et al [49] and D. Xia et al [50] to analyze the corrosion rate of metallic substrates at a fixed anodic potential of −500 mV/SCE in our case, a value taken within a range where the cathodic coating is considered inert (substrate dissolution through porosity. A significant decrease in the anodic current has been noticed, from 3.57 × 10^{-4} A/cm^2 for an uncoated substrate to a minimum value of 1.3 × 10^{-8} A/cm^2 for the coated substrate with 11 %.at incorporated Al-Ti-(W) coating. This decrease in corrosion current density, coupled with an increase in the anodic Tafel slope associated with the oxidation reaction of iron through the deposit porosities, could be explained by the densification of the Al—Ti deposit with tungsten addition.

Furthermore, for an applied potential higher than OCP intrinsic Al-Ti-(W) coatings (determined from Fig. 13), the contribution of these amorphous alloys were noticed with a sudden change in the anodic slope followed by the appearance of a passivation plateau. The results showed also that the incorporation of tungsten exerts a notable influence on the localized corrosion (pitting corrosion) behavior of the Al—Ti alloy, manifesting as a discernible increase in the pitting corrosion potential with tungsten addition.

The addition of 4 at.% W improved the linear polarization resistance from approximately 81.3 to 567.21 kΩ·cm^2. A shift in the corrosion potential to more negative values was observed, which was linked to a galvanic coupling between the metallic substrate and the coating through the open porosity. The incorporation of tungsten has been observed to enhance the pitting corrosion resistance of the Al—Ti alloy, where the pitting potential ranges from 173 to 432 mV/SCE. This suggests that tungsten affects the composition, nature, or structure of the passive layer formed on the alloy. A comparable observation has been reported for Ni—W alloys with increasing W content [48].

The incorporation of 11 at. % W significantly increased the linear polarization resistance after 1 h of immersion, reaching a value of approximately 1.66 MΩ·cm^2. This coating composition presented the most favorable corrosion resistance, as the addition of 17 at.% W resulted in a reduction in Rp, which may be attributed to the difference of multilayer structure mode obtained with tungsten incorporation for each coating composition, as previously mentioned in the first section of this paper.

Regarding the cathodic branch of the cyclic polarization curves for both the uncoated metallic substrate and those coated with Al-Ti-(W) thin films, the main electrochemical reaction produced at the electrode surface is the reduction of oxygen (RRO) in the aerated neutral electrolyte solution, expressed by the following reaction:

$$O_2 + 2H_2O + 4e^- \rightarrow 4OH^- \quad (2)$$

4.2.2. Al-Ti-(W) coated 100C6 steel behavior in long-term immersion

The evolutions of the open circuit potential and the polarization resistance Rp of the 100C6 substrate and the amorphous Al–Ti–(W) coatings as a function of immersion time are presented in Fig. 13 and Fig. 14.

The OCP of steel initially has a value of approximately – 0.5 V/SCE, which is consistent with the polarization test results presented previously. During immersion, the OCP of the steel shifts toward more negative values, then stabilizes after 5 h of immersion at about - 0.7 V/SCE. The corrosion products, generally formed as hydrated oxides and/or iron oxyhydroxides, progressively cover the substrate surface, reducing the access of dissolved oxygen to the metal and causing the OCP to shift toward the cathodic range. The Rp values are on the order of a few kΩ·cm^2 and evolve only slightly during immersion, suggesting that the corrosion products offer limited protection to the steel surface.

The reference Al—Ti coating exhibits an OCP evolution similar to that of the substrate. The OCP decreases from - 0.4 V/SCE to - 0.55 V/SCE and then remains stable during immersion. The decrease in potential indicates localized degradation of the substrate through open porosities. After several hours of immersion, the OCP shifts further toward negative values (−0.55 V/SCE). The initial Rp of the binary Al—Ti alloy is approximately 80 kΩ·cm^2, then drops abruptly to about 10–20 kΩ·cm^2. This rapid decrease is associated with localized corrosion of the substrate through open porosities. The formation of corrosion products within these pores slows the degradation of the substrate. However, the significant amount of open porosity makes the amorphous Al—Ti coating incapable of providing good corrosion protection and, in this

Table 5
Electrochemical parameters obtained from polarization curves of the metallic substrate and amorphous Al-Ti-(W) coatings after 1 h of immersion in NaCl solution.

Sample	100C6	0 at.% W	4 at.% W	11 at.% W	17 at.% W
E_{corr} (mV/SCE)	−662	−538	−606	−540	−734
i_{corr} (μA/cm^2)	3	0.3	0.05	0.01	0.03
*b*a (mV/dec)	73	80	144	157	193
i_{pass} (μA/cm^2)	–	80	30	20	30
E_{pit} (mV/SCE)		173	432	572	715
*R*p (kΩ. cm^2)	0.22	81.3	567.21	1666.66	100

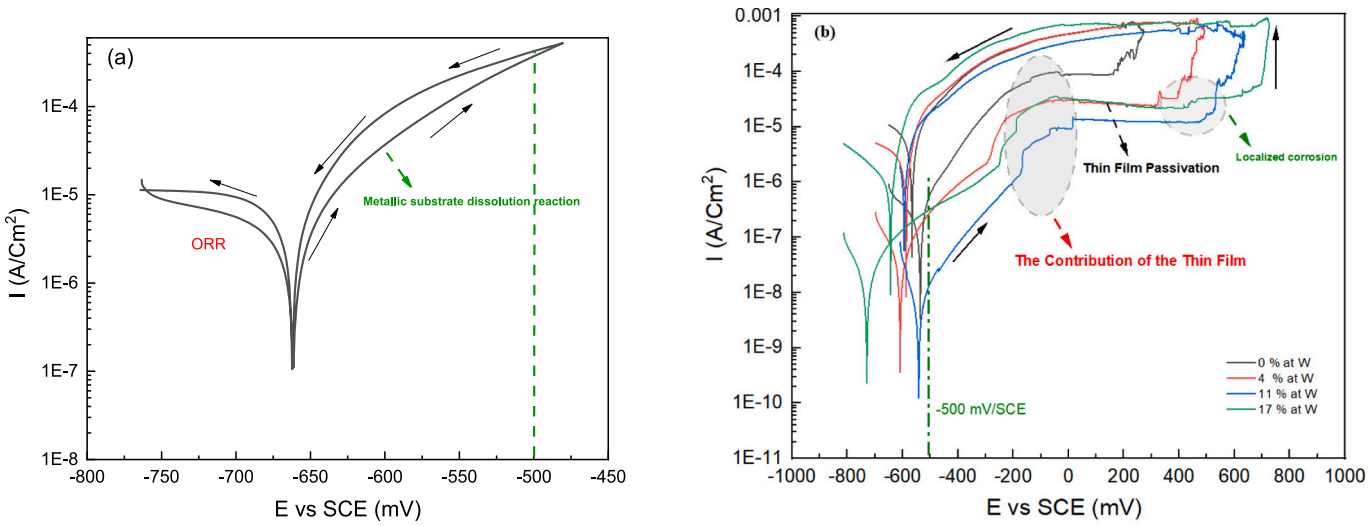

Fig. 12. Polarization curves of bare and Al-Ti-(W) coated 100C6 steel substrate after 1 h of immersion in NaCl: (a) bare steel, (b) Al-Ti-(W) coated steel.

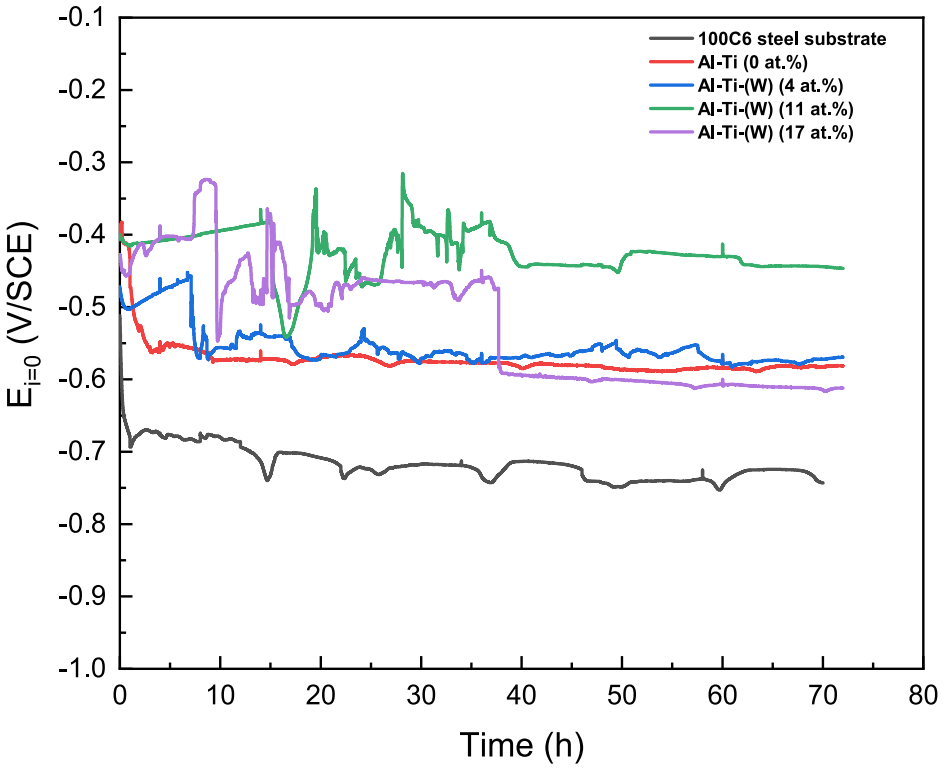

Fig. 13. Evolution of corrosion open circuit potential of the substrate and amorphous Al-Ti-(W) coatings as a function of immersion time in a saline environment.

case, promotes galvanic corrosion between the substrate and the thin coating layer.

The incorporation of tungsten into the Al–Ti–(W) coating completely changes the evolution of the OCP with immersion time. A shift of the potential toward more positive values is observed, indicating improved corrosion resistance of these ternary alloys, likely related to the densification induced by the addition of tungsten. The OCP of the Al–Ti–(W) alloy containing 4 at.% W starts at approximately - 0.5 V/SCE and then slightly ennobles to - 0.45 V/SCE after 6 h of immersion. Within this potential range, two phenomena may occur: localized corrosion of the substrate through defects and/or the formation of a passive film on the ternary alloy. The Rp values increase during this immersion period, reaching about 800 kΩ·cm^2 after 5 h, suggesting partial blocking of degradation within the open defects and/or partial passivation of the ternary film. After 7 h of immersion, a significant decrease in both OCP (toward more negative values) and Rp is observed, attributed to the onset of pitting and renewed localized corrosion of the steel through open porosity. It is noted that the Rp values eventually reach levels similar to those of the amorphous binary Al—Ti coating after 72 h of immersion.

For the Al–Ti–W (11 at. %) coating, ennoblement of the OCP is observed, increasing from −0.4 V/SCE at the beginning of immersion to −0.35 V/SCE after 13 h. The initial polarization resistance is close to 1500 kΩ·cm^2, indicating a low density of open defects due to the densification induced by tungsten incorporation. During the first 15 h of immersion, Rp values increase gradually up to 3000 kΩ·cm^2, reflecting

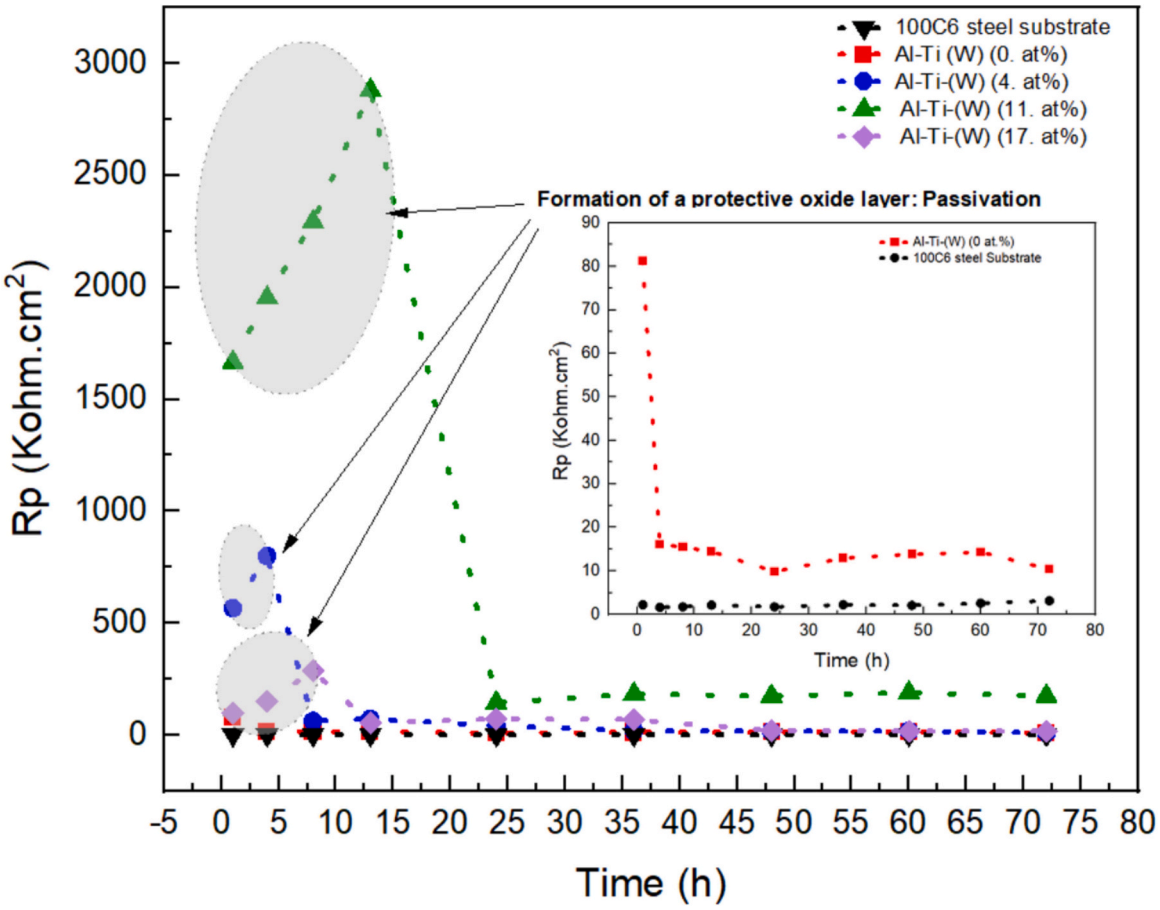

Fig. 14. Polarization resistance of the substrate and amorphous Al-Ti-(W) coatings as a function of immersion time in a saline environment.

the formation of a protective oxide film on the ternary alloy surface. After 13 h of immersion, pronounced potential oscillations appear, indicating the formation of through thickness defects and a competition between defect formation due to localized corrosion and the formation of the protective film, which could slow the activity of these defects. Despite the oscillations, the OCP remains close to - 0.4 V/SCE throughout immersion. After 13 h, Rp values decrease rapidly due to localized degradation of the ternary coatings and then stabilize at values still higher than those of the other compositions.

For the Al–Ti–(W (17 at.%)) coating, a similar behavior is observed, but with lower corrosion resistance compared to the Al–Ti–(W (11 at. %)) coating. During the first hours of immersion, the OCP increases toward more noble values, reaching - 0.32 V/SCE, which corresponds to a passivation potential. At the same time, Rp increases only slightly due to the formation of a protective film whose composition and/or structure appears to differ when the tungsten content is increased. After 10 h of immersion, the Rp values become comparable to those of the uncoated substrate, suggesting rapid dissolution of the latter through open defects.

These long-term immersion tests highlight the benefit of incorporating tungsten into the binary Al—Ti alloy. Densification reduces the amount of open defects and limits electrolyte penetration through them. In addition, the susceptibility to pitting corrosion is likely reduced by changes in the composition, nature, and/or structure of the passive film induced by tungsten incorporation, as previously reported in the works of M. Lagarde [51] and D. Figuet [48].

4.2.3. *Electrochemical impedance spectroscopy*

EIS was carried out during 72 h of immersion in a saline medium. In this section, two parameters will be investigated: the influence of immersion time, and the effect of tungsten incorporation into Al-Ti-(W) coatings.

4.2.3.1. Influence of immersion time. The effect of immersion time on the electrochemical reactivity of the exposed surface was assessed through the analysis of the data recorded after 1 h, 8 h, 24 h, and 72 h of immersion. The results are displayed in Figs. 15 and 16 as Nyquist and Bode plots.

The Nyquist diagram of the uncoated steel shows a capacitive loop associated with the corrosion of the steel upon immersion in the saline solution. During the initial hours of exposure, the diameter of the loop slightly decreases. This reduction may be attributed to changes in surface roughness caused by substrate corrosion, which leads to an increase in the number of reactive sites. After 24 h of immersion, the diameter of the capacitive loop gradually increases, likely due to the formation of corrosion products that hinder the diffusion of dissolved oxygen. The Bode diagram reveals a shift in the characteristic frequency of the capacitive loop, along with a decrease in phase angle with increasing immersion time, indicating surface coverage and increased roughness due to the accumulation of corrosion products.

For the reference Al—Ti amorphous coating, the Bode and Nyquist impedance diagrams are shown in Fig. 15(b). Regardless of the immersion time, the Nyquist diagram exhibits a single capacitive loop whose overall diameter decreases with increasing immersion time. The Bode diagram provides a clearer separation of the reaction mechanisms, allowing the identification of two time constants. A first process is detected in the high-frequency range (100–10 kHz), which is attributed to the response of the electrolyte within the coating porosities, while a second process appears in the mid-frequency range (0.1–10 Hz), corresponding to the charge transfer mechanism associated with the

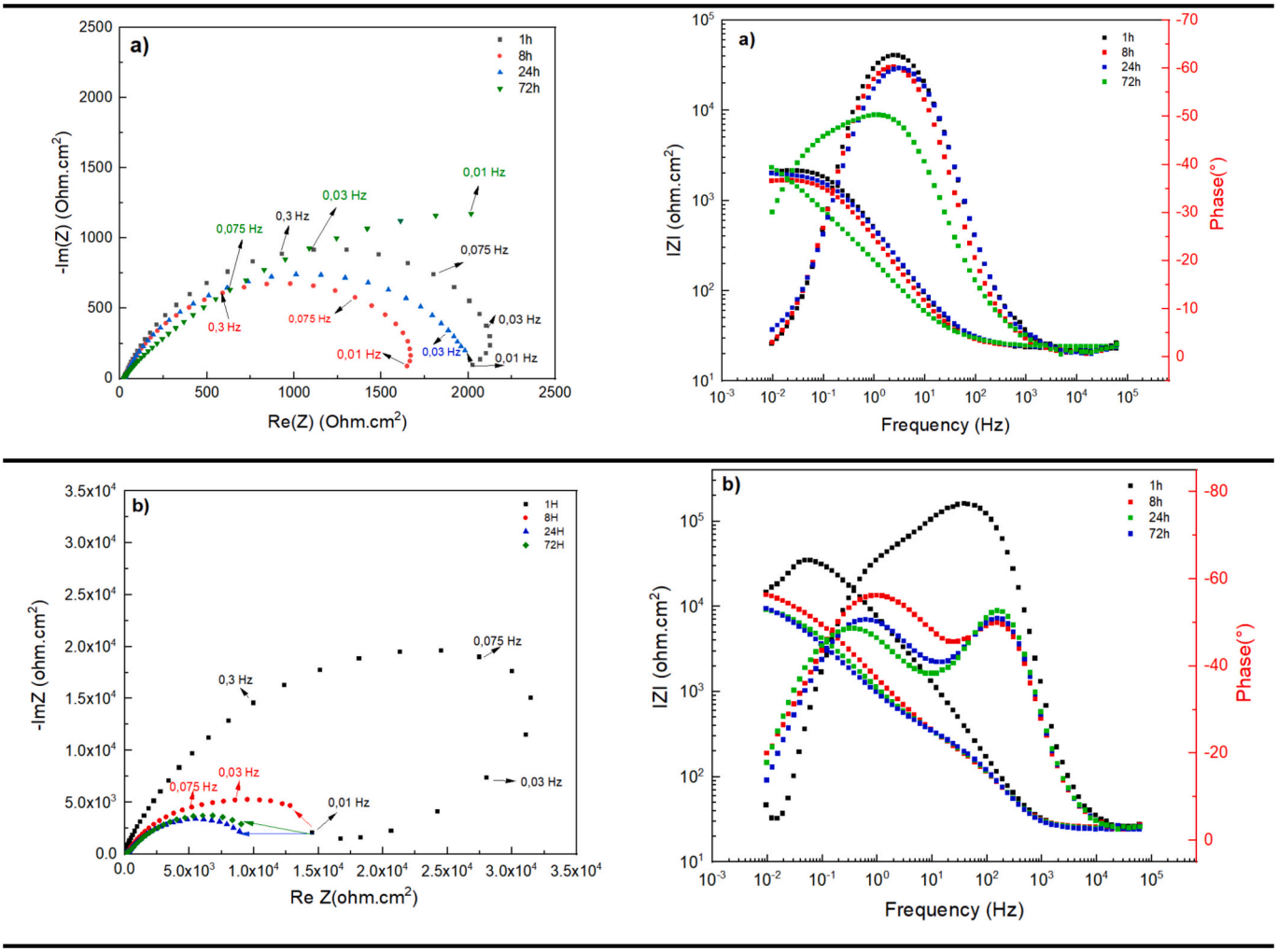

Fig. 15. Nyquist and Bode plots of the 100C6 metallic substrate (a) and the amorphous Al—Ti coating (b). Immersion times of 1 h, 8 h, 24 h, and 72 h.

oxidation of the substrate through the porosities.

After one hour of immersion, the diameter of the capacitive loop is approximately 40 kΩ·cm^2, which is of the same order of magnitude as the polarization resistance measurements. The diameter then decreases and stabilizes after 24 h of immersion at around 10 kΩ·cm^2. This trend is consistent with the evolution observed in the polarization resistance measurements.

Fig. 16 shows the evolution of the Nyquist and Bode plots for the Al—Ti coatings doped with tungsten at three compositions: 4, 11, and 17 at.% W.

For the composition containing 4 at.% W, the impedance diagrams exhibit a similar profile to that of the reference Al—Ti coating. After one hour of immersion, a very large capacitive loop with resistive behavior is observed in the Nyquist plot. The Bode diagram reveals two distinct time constants: one at high frequencies, corresponding to the response of the electrolyte within the film's porosities, and another at mid-frequencies, associated with the substrate's response through these defects. After one hour, the low-frequency impedance of the coated sample is estimated at approximately 500 kΩ·cm^2, consistent with the polarization resistance measurements. The incorporation of tungsten leads to a denser film with fewer defects. However, after 8 h of immersion, a significant decrease in low-frequency resistance is observed, indicating localized degradation of the substrate through open film defects. This decrease continues more gradually over time, eventually reaching values on the order of a few kΩ·cm^2. The localized corrosion of the substrate through these defects results in a change in the electrolyte composition within the cavities, accompanied by progressive acidification, which further accelerates the oxidation reaction.

For the coatings containing 11 at. % W, the Nyquist plots show a capacitive loop that indicates a resistive behavior of the coating up to 8 h of immersion. This behavior is attributed to the gradual formation of a passive layer. The Bode plots display a broad phase angle over a wide frequency range, revealing two time constants. These time constants are similar to those observed for the previously discussed coated samples. The resistive behavior increases during the first 8 h of immersion, likely due to the sealing of open pores by iron corrosion products and the formation of a passive film on the ternary coating. The initial low frequency impedance values are very high, confirming the strong effect of tungsten addition on the densification of the Al—Ti coating After 24 h of immersion, a decrease in impedance is observed, which may be related to the initiation and propagation of pitting corrosion on the surface of the ternary film and/or the reactivation of the substrate through pre-existing defects. It is worth noting that the low-frequency impedance value for the 11 at. % W ternary coating is around 100 kΩ.cm^2, indicating good corrosion resistance for this composition.

For the coatings containing 17 at.% W, the Nyquist plots also show a capacitive loop, indicating a resistive behavior of the coating after 1 h of immersion. The Bode plots display a broad phase angle over a wide frequency range, with two distinct time constants. From 8 h of immersion onward, a gradual decrease in the low frequency impedance is observed, indicating accelerated dissolution of the steel substrate through pre-existing defects or through defects created by the initiation

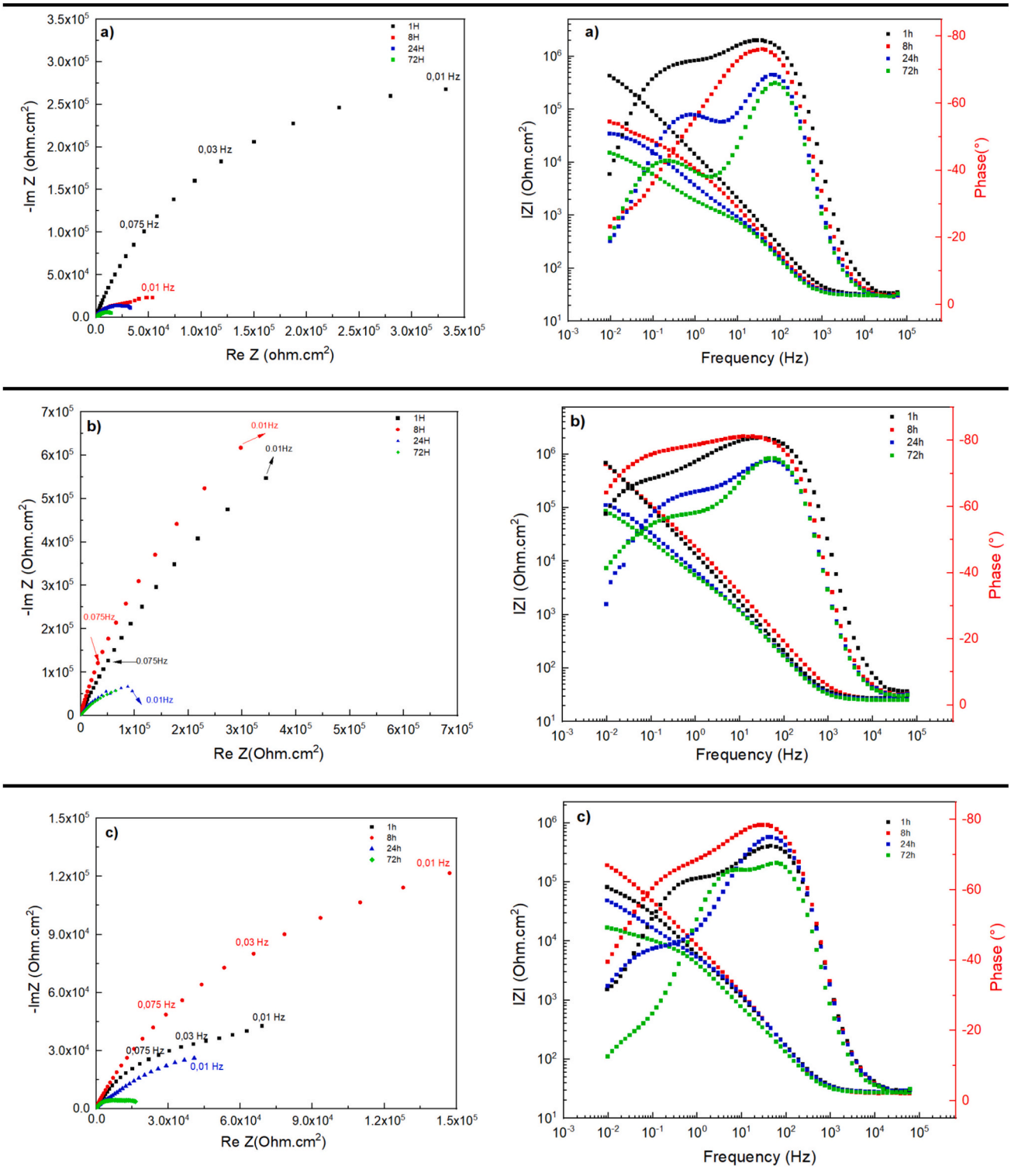

Fig. 16. Nyquist and Bode plots of Al-Ti-(W) coatings with 4 at.% (a), 11 at.% (b), and 17 at.% (c) W. Immersion times of 1 h, 8 h, 24 h, and 72 h.

and growth of pits on the ternary amorphous coating.

4.2.3.2. Influence of tungsten incorporation. The evolution of impedance with the incorporation of tungsten was investigated at different immersion times, specifically at 1 h, 8 h, and 72 h, as illustrated by the Nyquist plots shown.

in Fig. 17. These three immersion times allow us to better understand the behavior of Al-Ti-(W) coatings with different tungsten contents and to evaluate the performance of these coatings to protect the bare steel against corrosion. After 1 h of immersion, the corrosion process is mainly associated with the initial degradation of the coating surface. Depending on the size and number of open pores, the impact of localized substrate corrosion may remain limited at this early stage. After 8 h of immersion, physico-chemical phenomena begin to develop, including the formation of corrosion products such as oxide layers from the coating elements or steel corrosion products penetrating through

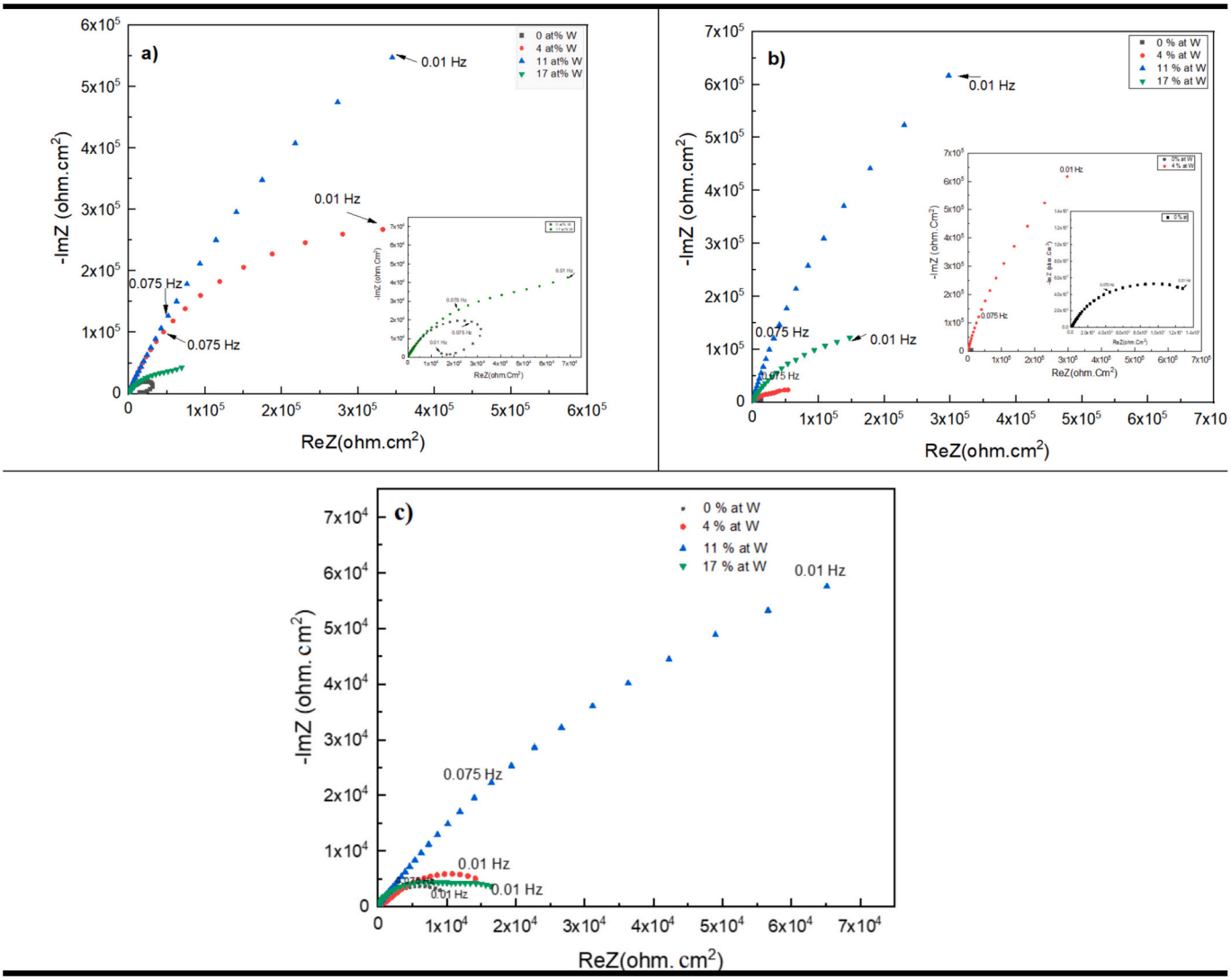

Fig. 17. Nyquist plots of amorphous Al-Ti-(W) coatings after 1 h (a), 8 h (b), and 72 h (c) of immersion in NaCl solution.

coating defects. After 72 h of immersion, the corrosion kinetics become more significant, as the exposure time is sufficient for substrate attack and for additional physico-chemical processes related to both coating and substrate corrosion products to develop.

After 1 h of immersion, tungsten incorporation improves the corrosion resistance of the coating. This is confirmed by the increase in the diameter of the capacitive loops with increasing tungsten content, reaching a maximum at 11 at. % W, indicating enhanced resistance to charge transfer at low frequencies. At 17 at.% W, a decrease in the capacitive loop diameter is observed, which may be attributed to additional factors such as pore density and pore depth. After 8 h of immersion, a similar behavior is observed, and the coating containing 11 at. % W exhibits the best corrosion resistance among the studied compositions. In contrast, the coating with 4 at. % W shows a significant decrease in impedance due to accelerated substrate corrosion through coating defects. After 72 h of immersion in the NaCl solution, the corrosion resistance of the Al—Ti, Al–Ti–(W (4 at. %)), and Al–Ti–(W (17 at. %)) coatings decreases markedly, and their capacitive loop diameters converge to similar values. The coating containing 11 at. % W still maintains good corrosion resistance, exhibiting a comparatively large capacitive loop diameter.

These results are consistent with the steady-state polarization resistance (Rp) measurements. They confirm that the degradation of the amorphous Al–Ti–(W) thin coatings in NaCl solution is primarily governed by two mechanisms: (i) the formation of oxide layers on the coating surface, and (ii) the evolution of porosity during immersion. These findings support the conclusions drawn from the polarization tests, which showed that tungsten incorporation increases the resistance to localized corrosion and decreases the passivation current, indicating the formation of a more protective oxide layer that slows down the substrate material degradation.

4.2.3.3. Modeling of EIS spectra of Al–Ti–(W)-coated steel. The impedance spectra were modeled using an equivalent electrical circuit (EEC) that describes the main processes at the electrode/electrolyte interface. The proposed model, shown in Fig. 18, allows extracting the key electrochemical parameters and tracking the evolution of corrosion during immersion.

It includes:

- **Re**: electrolyte resistance (ohmic drop).
- **Rpo**: pore electrolyte resistance, indicating the coating density and indirectly reflecting its multilayer structure.
- **CPE1**: constant phase element associated with the capacitive behavior of the coating.
- **CPE2**: constant phase element representing the response of the electrolyte solution/substrate interface inside the pores.

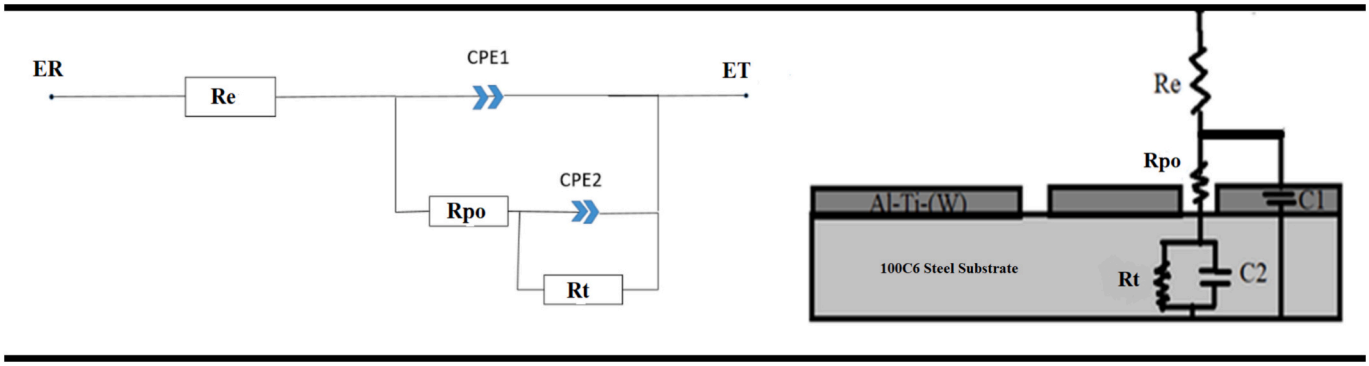

Fig. 18. Equivalent electrical circuit representing the behavior of Al-Ti-(W) coatings during long-term immersion (72 h).

- $\mathbf{R_T}$: charge transfer resistance, linked to substrate degradation and the development of protective oxide layers.

This model clarifies the role of each parameter and provides a better understanding of the coating's protective performance.

When charge transfer cannot be neglected, the effective capacitance of each CPE is calculated using the Brug relation [52], defined by the following equation:

$$C = Q^{\frac{1}{\alpha}}\left(Re^{(1-\alpha)} + Rp^{(1-\alpha)} \right)^{\frac{1}{\alpha}} \quad (3)$$

The electrochemical parameters obtained from modeling experimental data are presented in Table 6. The last column provides the parameter X2, which represents the modeling uncertainties and serves as a reliable indicator of the accuracy of the extracted parameters.

The electrolyte resistance associated with the saline solution ranges from 26 to 30 Ω·cm^2. These values remain nearly constant over the entire immersion period, confirming that the bulk chemical composition of the solution undergoes very little change during the degradation of the coated samples. The measured electrolyte resistance values are also consistent with those reported in the literature for a similar saline solution [52].

After 1 h of immersion, the Rpo of the Al–Ti-(W) coatings increases from 4050 to 39,146 Ω·cm^2 as the tungsten content increases from 0 to 11 at.%. This trend is consistent with the metallurgical characterizations, which indicated a densification of the binary coatings due to tungsten incorporation. For the ternary composition containing 17 at.% W, the Rpo value is the lowest, at approximately 2340 Ω·cm^2. This is explained by the multilayer growth mode induced by tungsten incorporation in each composition, as discussed in the first section.

The Rpo values gradually decrease during immersion time, indicating more active localized corrosion of the substrate through defects. In the case of the amorphous Al—Ti alloy, Rpo decreases from 4050 to 212 Ω·cm^2 after 8 h of immersion. A similar evolution is observed for the Al–Ti–(W) containing 4 at.% W, for which the electrolyte resistance drops sharply from 15,033 to 2044 Ω·cm^2 during the first 8 h of immersion, then Rpo decreases more gradually, likely due to the opening or propagation of new surface defects. For the ternary alloy with 11 at. % tungsten, an increase in Rpo occurs during the first hours of immersion, rising from 39,146 to 46,903 Ω·cm^2. This configuration presents a low porosity or small open pores that become partially sealed by the combined action of corrosion product formation on the substrate and the

Table 6
Electrochemical parameters derived from the modeling of electrochemical impedance spectra.

AlTiW(0 %)	Re (Ω.cm^2)	Rpo (Ω.cm^2)	Rt (Ω.cm^2)	Q1 .10^{-5} (F.S$^{(\alpha)}$)	α1	C1 (μF.cm^{-2})	Q2 .10^{-4} (F.S$^{(\alpha)}$)	α2	C2 (μF.cm^{-2})	X^2 (.10^{-4})
1H	25	4050	60,238	1.37	0.92	21.5	0.26	0.66	36.3	0.83
8H	25	212	15,902	2.18	0.91	32	1.6	0.7	289	1.1
24H	24	295	10,580	2.89	0.88	38.5	2.4	0.71	439.1	3
72H	25	350	16,800	2.6	0.89	36.7	2.6	0.68	618.4	7.9

AlTiW(4 %)	Re (Ω.cm^2)	Rpo (Ω.cm^2)	Rt (Ω.cm^2)	Q1 .10^{-5} (F.S$^{(\alpha)}$)	α1	C1 (μF.cm^{-2})	Q2 .10^{-4} (F.S$^{(\alpha)}$)	α2	C2 (μF.cm^{-2})	X^2.10^{-4}
1H	31	15,033	709,330	0.96	0.92	17	0.07	0.72	14.2	0.69
8H	31	2044	125,870	1.26	0.94	21.5	0.73	0.42	1591.4	9.24
24H	31	1337	41,485	1.51	0.94	25	6.36	0.71	2855.6	2.23
72H	30	1063	19,911	1.78	0.93	27.9	20.83	0.66	16,625.5	1.3

AlTiW(11 %)	Re (Ω.cm^2)	Rpo (Ω.cm^2)	Rt (Ω.cm^2)	Q1 .10^{-5} (F.S$^{(\alpha)}$)	α1	C1 (μF.cm^{-2})	Q2 .10^{-4} (F.S$^{(\alpha)}$)	α2	C2 (μF.cm^{-2})	X^2.10^{-4}
1H	26	39,146	1,534,000	0.81	0.93	15.4	0.0059	0.66	0.88	1.7
8H	27	46,903	35,366,001	1.16	0.94	22.5	0.04	0.68	14.4	0.92
24H	26	2809	197,790	1.45	0.93	24.9	0.27	0.66	68.7	4.68
72H	25	2447	249,540	1.43	0.94	25.2	0.47	0.61	237.2	0.8

AlTiW(17 %)	Re (Ω.cm^2)	Rpo (Ω.cm^2)	Rt (Ω.cm^2)	Q1 .10^{-5} (F.S$^{(\alpha)}$)	α1	C1 (μF.cm^{-2})	Q2 .10^{-4} (F.S$^{(\alpha)}$)	α2	C2 (μF.cm^{-2})	X^2.10^{-4}
1H	27	2337	111,630	1.58	0.92	26.1	0.31	0.65	65.7	3.2
8H	26	7357	386,290	1.47	0.94	26.4	0.17	0.63	53.7	1.4
24H	27	4070	115,650	1.56	0.93	26.3	0.74	0.57	392.1	1.35
72H	27	573	12,991	1.70	0.94	27	0.42	0.65	35.9	7.1

passive layer on the Al–Ti–(W) alloy. After 24 h of immersion, the Rpo values indicate active localized corrosion of the substrate through the defects. For the ternary alloy with 17 at. % tungsten, the Rpo values show the presence of a high density of small defects, which can be sealed during the first hours of immersion by the same combined actions.

The charge transfer resistance (Rt) shows a trend similar to Rpo. The Al–Ti–(W) coatings (11 at. % and 17 at. %) exhibit an increase in Rt during the first hours of immersion, which contributes to protecting the substrate surface. The Rt values obtained from the model, which represent the low frequency impedance of the system, are consistent with the polarization resistance values measured under steady-state conditions.

The capacitance C1 corresponds to the film capacitance, with values between 14 and 37 μF/cm^2. Its increase over immersion time is related to the formation of oxide layers on the Al–Ti–(W) coating. The parameter α1 remains close to 1 (between 0.88 and 0.94), indicating that the coating surface is homogeneous and only slightly rough [36].

The capacitance C2 represents the electrochemical double layer at the electrolyte/steel substrate interface through the open porosity in the confined environment. The values of C2 also increase with immersion time for all Al–Ti–(W) coatings. This indicates the formation of iron corrosion products in the confined medium and suggests that diffusion plays an important role in transporting electroactive species to the interface. The α2 values range from 0.5 to 0.7, reflecting strong heterogeneities in charge distribution due to pore morphology or diffusion effects.

In summary, the electrical model shown in Fig. 18 describes well the reaction steps and their evolution during long-term immersion in saline solution. The amorphous Al—Ti coatings are nobler than the substrate, so degradation is mainly controlled by defects that reach the substrate and by the resulting galvanic coupling. Adding tungsten to the Al—Ti alloy makes the coating denser by reducing the number of paths available for electrolyte penetration, due to a multilayer growth mode. This improves the localized corrosion resistance of the coating during long-term immersion.

4.2.4. Observation and analysis of corrosion products

The surface exposed (outlined in black) to the saline environment was examined after 72 h of immersion using optical microscopy, as shown in Fig. 19. The surface of the steel shows uniform material degradation, manifested by the formation of orange corrosion products on the surface and a rather “black” layer in the inner layer.

The corrosion of the Al—Ti coated substrate was observed through the presence of circular-shaped pits distributed across the surface exposed to the saline environment. The optical observations correlate well with the impedance test results discussed in the previous section, where the number and size of the pits vary depending on the composition of the film. Tungsten addition induces a reduction in pit size from an average value of 600 μm to 150 μm for a tungsten content of 11 %, as shown in Fig. 19. The pit size in the Al-Ti-(W (17 % at.)) coating increased, suggesting a decline in the performance of the ternary Al-Ti-(W) coating. The pit periphery reveals the presence of black corrosion products, which are oxide products resulting from substrate dissolution through the pits during electrolyte infiltration through the coating.

4.2.5. Corrosion products identification after long-term immersion

After 72 h of immersion in the saline solution, the corrosion products formed on the exposed surface of 1 cm^2 (the area outlined in black in Fig. 19) were analyzed by Raman spectroscopy (Fig. 20).

For the reference binary Al—Ti coating, the areas analyzed within the porosities and around the defects exhibit similar Raman spectra (Fig. 20.a). These spectra show low-intensity vibrational bands at 324 cm^{-1} and 540 cm^{-1}, along with an intense band at 665 cm^{-1}. According to the literature, these vibrational bands are characteristic of an iron oxide known as magnetite (Fe_3O_4) [53]. These dark, blackish oxides typically form under conditions of low oxygen content and a rather basic pH [54], resulting from cathodic reduction reactions of dissolved oxygen occurring primarily on the surface of the Al—Ti alloy.

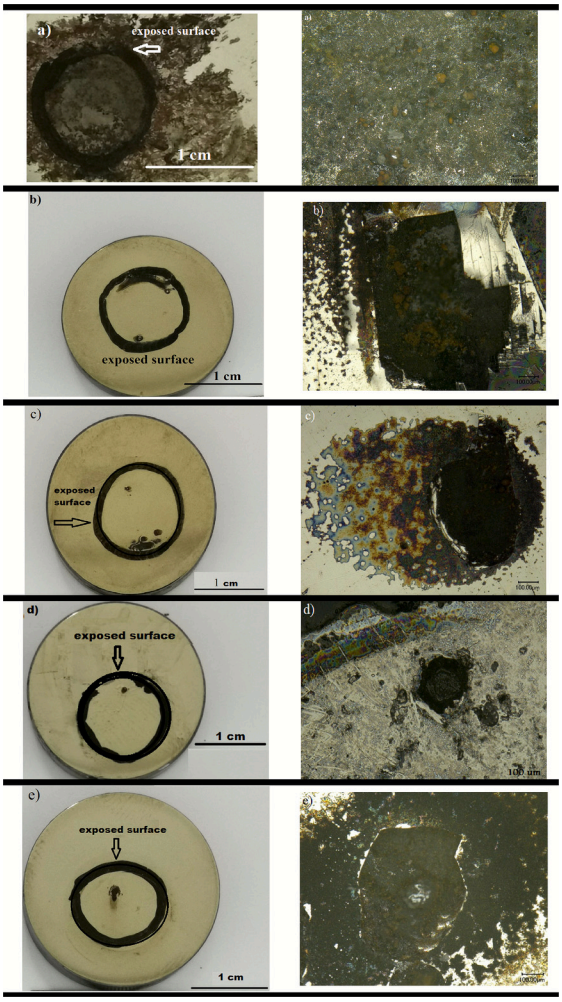

Fig. 19. Optical observations of the exposed surface after long-term immersion tests: (a) substrate; amorphous coatings: (b) Al–Ti; (c) Al–Ti–W (4 at.%); (d) Al–Ti–W (11 at.%); and (e) Al–Ti–W (17 at.%).

In Fig. 20.b, the Raman spectra obtained for the ternary Al-Ti-(W = 4 at.%) coating reveal the presence of magnetite in the areas surrounding the pits. Inside the pits, the spectrum exhibits a different profile, with bands observed at 304 cm^{-1}, 383 cm^{-1}, 407 cm^{-1}, 533 cm^{-1}, 670 cm^{-1}, and 716 cm^{-1}. These bands are characteristic of magnetite and akaganeite (β-FeOOH) [53], the latter compound typically forming under high chloride concentrations [55]. The incorporation of 11 at.% W in the coating results in shallower pits and defects compared to other compositions. The Raman spectrum recorded inside these defects shows the absence of corrosion products. Around and away from these defects, a spectrum containing three bands at 268.5 cm^{-1}, 707 cm^{-1}, and 1079 cm^{-1} was detected; this corrosion product may be associated with a tungsten oxide of the WO_3 type [56], which supports the hypothesis of a protective passivation layer forming during immersion. Fig. 20.d displays the Raman spectrum of corrosion products from the Al-Ti-(W) coating containing 17 at.% W. Around the pits, the spectrum exhibits vibrational bands at 245 cm^{-1}, 297 cm^{-1}, 377 cm^{-1}, 392 cm^{-1}, 528 cm^{-1}, and 665 cm^{-1}, characteristic of a mixture of lepidocrocite and magnetite [57]. The same corrosion products were identified inside the visible pits, indicating their propagation through to the metallic substrate during the 72-h immersion.

In regards to the electrochemical behavior and the results, the open circuit potential indicate that the Al-Ti-(W) amorphous thin films exhibit

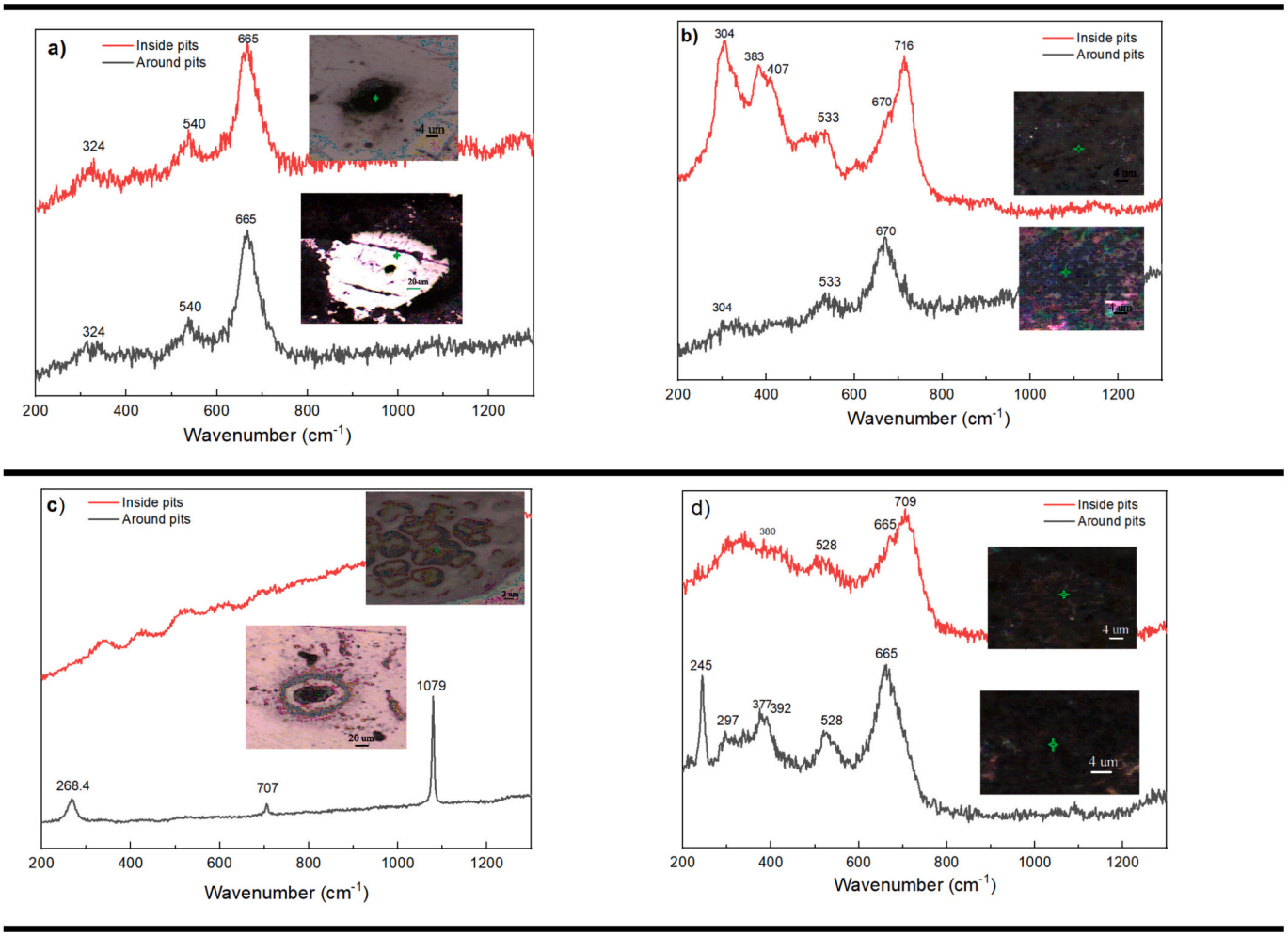

Fig. 20. Raman spectra of corrosion products from metallic substrates coated with Al–Ti–(W) alloys: (a) 0 %, (b) 4 %, (c) 11 %, and (d) 17 at.% W, after long-term immersion tests (72 h).

cathodic protection against corrosion degradation. Therefore, the quality of the film growth and its morphology play a crucial role as corrosion barriers. To be more precise, the degree of porosity and the chemical composition of the elements constituting the amorphous thin films are the factors that influence their corrosion resistance. Fig. 21 provides a summary of how the incorporation of tungsten enhances the thin film resistance against environmental attack. The XRD and TEM microstructure analysis indicated that as the concentration of tungsten in the film increases, the film becomes more dense. In addition, the multilayer growth obtained with tungsten incorporation helps to reduce cloride diffusion pathways, such as open pores and defects. The multilayered microstructure also helps to block and stop the growth of porosities and cracks during the elaboration process by creating interfaces and nucleating new growth sites when tungsten is sputtered.

5. Conclusion

This paper presents the development of a new Al-Ti-(W) amorphous thin film using magnetron co-sputtering PVD technology on 100C6 metallic substrates. Firstly, the study investigated, the thin films characterization such as the structure, the microstructure, and morphology at both micrometric and nanometric scales. The results indicate that a

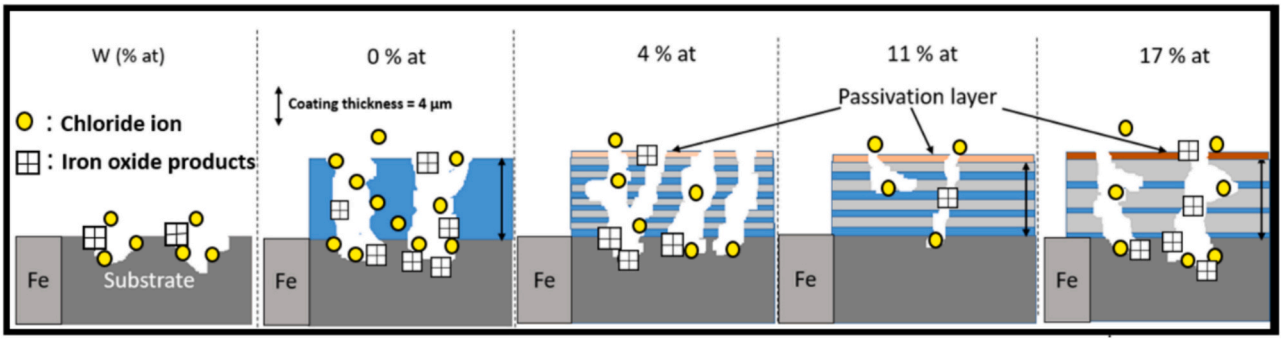

Fig. 21. Evolution of metallurgical and electrochemical parameters as a function of tungsten content in amorphous Al-Ti-(W) coatings.

homogeneous, dense coating was achieved at the micrometric scale while a nano-multilayered microstructure with 2.9 nm periodic growth revealed a non-homogeneous tungsten distribution. A new experimental method was developed to understand the multilayer growth mechanism observed at 17 at.% of tungsten incorporation through transmission microscopy. This method, confirmed by simulation approach, was also used to determine the growth mode for other compositions. OCP tests confirmed cathodic protection during galvanic coupling with 100C6 steel, with higher OCP values for the thin films compared to the substrate. The electrochemical investigations, complemented by impedance modeling, demonstrate that tungsten incorporation markedly enhances the corrosion resistance of amorphous Al—Ti coatings deposited on 100C6 steel. Modeling of the EIS spectra highlights a significant increase in pore resistance (Rpo) with W addition, evidencing coating densification that is likely associated with the multilayer growth mode previously identified in the microstructural analysis. This densification reduces the number and connectivity of open defects, limits electrolyte penetration, and promotes the formation of protective oxide layers, leading to lower corrosion currents and higher impedance and polarization resistance. Among all compositions, the Al–Ti–(W) coating containing 11 at.% W offers the best protection against corrosion. The overall trend confirms the beneficial role of W in controlling porosity driven degradation. In an amorhpous state,these results underline the potential of W modified amorphous Al—Ti coatings for improved durability in chloride-rich environments.

CRediT authorship contribution statement

Issam Lakdhar: Writing – original draft, Methodology, Investigation, Formal analysis, Data curation, Conceptualization. **Akram Alhussein:** Writing – review & editing, Resources, Project administration. **Jean-Luc Grosseau-Poussard:** Writing – review & editing. **Corinne Nouveau:** Writing – review & editing. **Aurélien Besnard:** Writing – review & editing, Methodology. **Juan Creus:** Validation, Supervision, Formal analysis, Conceptualization.

Declaration of competing interest

The authors declare that they have no known competing financial interests or personal relationships that could have appeared to influence the work reported in this paper.

Data availability

Data will be made available on request.

Acknowlegments

The authors would like to thank Mr. Fabrice Parent, Technician at the UTT, for his help in PVD machine preparation, and Mr. Jaafar Ghanbaja, Research engineer at IJL Nancy, for performing TEM analyses.

The authors would like to thank the European Union (FEDER – Fond Européen de Développement Régional), co-funder of DERBHY project, also the GIP52 (Groupement d'Intérêt Public Haute-Marne) for their financial support.

References

[1] Ch. Verma, Eno E. Ebenso, M.A. Quraishi, Corrosion inhibitors for ferrous and non-ferrous metals and alloys in ionic sodium chloride solutions: a review, J. Mol. Liq. 248 (2017) 927–942.
[2] Y. Yang, F. Khan, P. Thodi, R. Abbassi, Corrosion induced failure analysis of subsea pipelines, in: Reability Engineering and Safety System 159, 2017, pp. 214–222.
[3] https://www.g2mtlabs.com/cost-of-corrosion/.
[4] G.H. Koch, M.P.H. Brongers, N.G. Thompson, Corrosion costs and preventive strategies in the united states, in: FHWA (Federal Highway Administration)-RD-01-156, 2002. R315–01.
[5] K.R. Trethewey, D.R. Roberge, Corrosion management in 21th century, Br. Corros. J. 30 (1995) 192–197.
[6] K.D. Ralston, N. Birbilis, C.H.J. Davies, Revealing the relationship between grain size and corrosion rate of metals, Scr. Mater. 63 (2010) 1201–1204.
[7] K.D. Ralston, N. Birbilis, M. Weyland, C.R. Hutchinson, The effect of precipitate size on the yield strength-pitting corrosion correlation in Al–Cu–Mg alloys, Acta Mater. 58 (2010) 5941–5948.
[8] K.D. Ralston, N. Birbilis, M.K. Cavanaugh, M. Weyland, B.C. Muddle, R.K. W. Marceau, Role of nanostructure in pitting of Al–Cu–Mg alloys, Electrochem. Acta 55 (2010) 7834–7842.
[9] K.D. Ralston, D. Fabijanic, N. Birbilis, Effect of grain size on corrosion of high purity aluminium, Electrochem. Acta 56 (2011) 1729–1736.
[10] J.G. Brunner, N. Birbilis, K.D. Ralston, S. Virtanen, Impact of ultrafine-grained microstructure on the corrosion of aluminium alloy AA2024, J. Corros. Sci. 57 (2012) 209–214.
[11] R. Lindsay, S.B. Lyon, Introduction to control of corrosion by environmental modification, Shreir's, Corrosion 4 (2010) 2891–2899.
[12] W. Xu, Yi Chen, Li Chen, H. Huang, Ch. Li, Effect of cathodic protection potential change caused by alternating current interference on corrosion behavior of X90 steel in 3% NaCl solution, Int. J. Electrochem. Sci. 17 (2022) 221019.
[13] S. Trujillo, R. Reyes-Riverol, F.R. Garcia-Galvan, S. Fajardo, New electrochemical method for the determination of the barrier properties of corrosion protective coatings, Prog. Org. Coat. 190 (2024) 108390.
[14] L. Zhang, X. Liu, J. Yan, Preparation of superhydrophobic coating with anti-corrosion and anti-fouling properties on the surface of low manganese steel by electrodeposition, Surf. Coat. Technol. 460 (2023) 129412.
[15] F. Yu, L. Camilli, T. Wang, D.A. Mackenzie, M. Curioni, R. Akid, P. Bøggild, Complete long-term corrosion protection with chemical vapor deposited graphene, Carbon 132 (2018) 78–84.
[16] I. Berdoyes, H. Plaisantin, J. Danet, The corrosion behavior of various CVD SiC coatings in molten silicon, Ceram. Int. 50 (2024) 3877–3886.
[17] E. Marin, A. Lanzutti, L. Guzman, L. Fedrizzi, Corrosion protection of AISI 316 stainless steel by ALD alumina/titania nanometric coatings, J. Coat. Technol. Res. 8 (2011) 655–659.
[18] E. Kaady, R. Habchi, M. Bechelany, E. Zgheib, A. Alhussein, Effect of Al2O3, ZnO and TiO2 atomic layer deposition grown thin films on the electrochemical and mechanical properties of sputtered Al-Zr coating, Coatings 13 (2023) 65.
[19] H. Hoche, C. Pusch, M. Oechsner, Establishing PVD-coatings for the corrosion protection of mild steel substrates for complex tribological and corrosive stresses, Surf. Coat. Technol. 376 (2019) 74–83.
[20] E. Kaady, A. Alhussein, M. Bechelany, R. Habchi, Al2O3-ZnO atomic layer deposited nanolaminates for improving mechanical and corrosion properties of sputtered CrN coatings, Thin Solid Films 759 (2022) 139476.
[21] M. Noori, M. At Apour, M. Ashrafizadeh, Nanostructured multilayer CAE-PVD coatings based on transition metal nitrides on Ti6Al4V alloy for biomedical applications, Ceram. Int. 49 (2023) 23367–23382.
[22] M. Stueber, H. Holleck, H. Leiste, K. Seemann, S. Ulrich, C. Ziebert, Concepts for the design of advanced nanoscale PVD multilayer protective thin films, J. Alloys Compd. 483 (2009) 321–333.
[23] K. Aouadi, B. Tlili, C. Nouveau, A. Besnard, M. Chafra, R. Souli, Influence of substrate bias voltage on corrosion and wear behavior of physical vapor deposition CrN coatings, J. Mater. Eng. Perform. 28 (2019) 2881–2891.
[24] L.A. Dobrzański, K. Lukaszkowicz, D. Paku, J. Miku, Corrosion resistance of multilayer and gradient coatings deposited by PVD and CVD techniques, Arch. Mater. Sci. Eng. 28 (2007) 12–18.
[25] J. Creus, C. Berziou, S. Cohendoz, A. Perez, C. Rébéré, M. Reffass, S. Touzain, C. Allely, Y. Gachon, C. Héau, F. Sanchette, A. Billard, Reactivity classification in saline solution of magnetron sputtered or EBPVD pure metallic, nitride and Al-based alloy coatings, Corros. Sci. 57 (2012) 162–173.
[26] B.R. Braeckman, D. Depla, On the amorphous nature of sputtered thin film alloys, Acta Mater. 109 (2016) 323–329.
[27] A. Inoue, Stabilization of metallic supercooled liquid and bulk amorphous alloys, Acta Mater. 48 (2000) 279–306.
[28] C.W. Chu, Jason S.C. Jang, S.M. Chiu, J.P. Chu, Study of the characteristics and corrosion behavior for the Zr-based metallic glass thin film fabricated by pulse magnetron sputtering process, Thin Solid Films 517 (2009) 4930–4933.
[29] B. Subramanian, In vitro corrosion and biocompatibility screening of sputtered $Ti_{40}Cu_{36}Pd_{14}Zr_{10}$ thin film metallic glasses on steels, Mater. Sci. Eng. C 47 (2015) 48–56.
[30] M. Apreutesei, C. Boissy, N. Mary, M. Arab Pour Yazdi, A. Billard, P. Steyer, Binary Zr–Ni/Co metallic glass films: role of the structural state on their durability, Acta Mater. 89 (2015) 305–314.
[31] Q. Yan, H. Yoshioka, H. Habazaki, A. Kawashima, K. Asami, K. Hashimoto, The pitting corrosion of sputter-deposited amorphous Al-Ti alloys in neutral chloride-containing solution, J. Non Cryst. Solids 125 (1990) 25–31.
[32] E. Abe, M. Ohnuma, M. Nakamura, The structure of a new ε phase formed during the early stage of crystallization of Ti-48 at. % Al amorphous film, Acta Mater. 47 (1999) 3607–3616.
[33] O.N. Senkov, M.D. Uchic, S. Menon, D.B. Miracle, Crystallisation kinetics an amorphous AlTi sheet produced by PVD, Scr. Mater. 46 (2002) 187–192.
[34] H.C. Kim, N.D. Theodore, K.S. Gadre, J.W. Mayer, T.L. Alford, Investigation of thermal stability, phase formation, electrical and microstructural properties of sputter-deposited titanium aluminide thin films, Thin Solid Films 460 (2004) 17–24.

[35] F. Sanchette, A. Billard, Main features of magnetron sputtered aluminium–transition metal alloy coatings, Surf. Coat. Technol. 142-144 (2001) 218–224.
[36] I. Lakdhar, A. Alhussein, J. Capelle, J. Creus, Al-Ti-(W) alloys deposited by magnetron sputtering: effective barrier to prevent steel hydrogen embrittlement, Appl. Surf. Sci. 567 (2021) 150786.
[37] R. Kowong, S. Denchitcharoen, T. Lertvanithphol, N. Triamnak, C. Chananonnawathorn, Structural and mechanical behavior of Zr-W-Ti thin film metallic glasses prepared by multitarget co-magnetron sputtering, J. Alloys Compd. 936 (2023) 168330.
[38] C. Lo, P. McDonald, D. Draper, P. Gilman, Influence of tungsten sputtering target density on physical vapor deposition thin film properties, J. Electron. Mater. 34 (2005) 1468–1473.
[39] J.-C. Chang, J.-W. Lee, B.-S. Lou, C.-L. Li, J.P. Chu, Effects of tungsten contents on the microstructure, mechanical and anticorrosion properties of Zr–W–Ti thin film metallic glasses, Thin Solid Films 584 (2015) 253–256.
[40] J. Zhao, Z. Jiang, C. Lee, Effects of tungsten on the hydrogen embrittlement behavior of microalloyed steels, Corros. Sci. 82 (2014) 380–391.
[41] W. Püttgen, B. Hallstedt, W. Bleck, J.F. Löffler, P.J. Uggowitzer, On the microstructure and properties of 100Cr6 steel processed in the semi-solid state, Acta Mater. 55 (2007) 6553–6560.
[42] D. Depla, W.P. Leroy, Magnetron Sputter Deposition as Visualized by Monte Carlo Modeling, Thin Solid Film Vol. 520, 2012, pp. 6337–6354.
[43] O.P. Rachek, X-ray diffraction study of amorphous alloys Al–Ni–Ce–Sc with using Ehrenfest's formula, J. Non Cryst. Solids 352 (2006) 3781–3786.
[44] A. Billard, F. Perry, Pulvérisation cathodique magnétron, Techniques de l'ingénieur 1 (2005). M1654 V1.
[45] Y. Zou, J. Wang, Q. Bai, L.L. Zhang, X. Peng, X.F. Kong, Potential distribution characteristics of mild steel in seawater, Corros. Sci. 57 (2012) 202–208.
[46] J. Creus, H. Idrissi, H. Mazille, Galvanic corrosion behaviour of mild steel, Al and Ti in 3%NaCl solution: application to PVD coatings on steel substrate, Surf. Eng. 13 (1997) 415–419.
[47] A. Perez, F. Sanchette, A. Billard, C. Rébéré, C. Berziou, S. Touzain, J. Creus, Comparison of the intrinsic properties of EBPVD Al–Ti and Al–Mg coatings, Mater. Chem. Phys. 132 (2012) 154–161.
[48] D. Figuet, Thesis. Relations entre structures, comportements à la corrosion et propriétés Tribologiques des revêtements de NixW1-x, LaSie laboratory, Rochelle University, 2020.
[49] M. Hou, C. Pan, M. Wang, D. Xia, Z. Qin, W. Hu, Improving the cavitation corrosion resistance of 6061 aluminum alloy by anodizing, Electrochim. Acta 503 (2024) 144890.
[50] D. Xia, C. Deng, D. Macdonald, S. Jamali, D. Mills, J. Luo, M.G. Strbel, M. Amiri, W. Jin, S. Song, W. Hu, Electrochemical measurements used for assessment of corrosion and protection of metallic materials in the field: a critical review, J. Mater. Sci. Technol. 112 (2022) 151–183.
[51] M. Lagarde, Thesis, Relations among Elaboration Process, Metalurgical State and Proprieties of Nanostructured Alloy Ni-W, LaSie Laboratory, Rochelle University, 2017.
[52] G.J. Brug, A.L.G. Van den edden, M. Sluyters-Rehbach, J.H. Sluyters, The analysis of electrode impedances complicated by the presence of a constant phase element, J. Electroanal. Chem. Interfacial Electrochem. 176 (1984) 275–295.
[53] P. Colomban, S. Cherifi, G. Despert, Raman identification of corrosion products on automotive galvanized steel sheets, J. Raman Spectrosc. 39 (2008) 881–886.
[54] P. Roonasi, A. Holmgren, A study on the mechanism of magnetite formation based on iron isotope fractionation, conference paper Warrendale (USA), Minerals, Metals & Materials Society (2009) 829–836.
[55] Y. Cudennec, A. Lecerf, Étude des mécanismes de formation des oxy-hydroxydes de fer; hypothèses de transformations topotactiques, C.R. Chimie 6 (2003) 437–444.
[56] A. Baserga, V. Russo, F. Di Fonzo, A. Bailini, D. Cattaneo, C.S. Casari, A. Li Bassi, C. E. Bottani, Nanostructured tungsten oxide with controlled properties: synthesis and Raman characterization, Thin Solid Films 515 (2007) 6465–6469.
[57] S.J. Oh, D.C. Cook, H.E. Townsend, Characterization of Iron oxides commonly formed as corrosion products on steel, Hyperfine Interact. 112 (1998) 59–66.